INTERNATIONAL JOURNAL FOR NUMERICAL AND ANALYTICAL METHODS IN GEOMECHANICS
Int. J. Numer. Anal. Meth. Geomech. 2013; **37**:2427–2455
Published online 5 October 2012 in Wiley Online Library (wileyonlinelibrary.com). DOI: 10.1002/nag.2142

Fibre reinforced sands: from experiments to modelling and beyond

A. Diambra[1,*,†], E. Ibraim[1], A. R. Russell[2] and D. Muir Wood[3]

[1]*University of Bristol, Bristol, U.K.*
[2]*The University of New South Wales, Sydney, Australia*
[3]*University of Dundee, Dundee, U.K.*

SUMMARY

Based on hypotheses derived directly from experimental observations of the triaxial behaviour, a constitutive model for fibre reinforced sands is built in this paper. Both the sand matrix and the fibres obey their own constitutive law, whereas their contributions are superimposed using a volumetric homogenization procedure. The Severn-Trent sand model, which combines well-known concepts such as critical state theory, Mohr-Coulomb like strength criterion, bounding surface plasticity and kinematic hardening, is adopted for the sand matrix. Although the fibres are treated as discrete forces with defined orientation, an equivalent continuum stress for the fibre phase is derived to allow the superposition of effects of sand and fibres. The fibres are considered as purely tensile elements following a linear elastic constitutive rule. The strain in the fibres is expressed as a fraction of the strain in the reinforced sample so that imperfect bonding is assumed at the sand-fibre interface. Only those fibres oriented within the tensile strain domain of the sample can mobilize tensile stress—the orientation of fibres is one of the key ingredients to capture the anisotropic behaviour of fibre reinforced soil that is observed for triaxial compression and extension loading. A further mechanism of partition of the volume of voids between the fibres and the sand matrix is introduced and shown to be fundamental for the simulation of the volumetric behaviour of fibre-reinforced soils. Copyright © 2012 John Wiley & Sons, Ltd.

Received 16 January 2012; Revised 3 July 2012; Accepted 27 July 2012

KEY WORDS: soil reinforcement; sand; fibre; constitutive modelling; laboratory testing

1. INTRODUCTION

Soil materials are widely used to build geotechnical systems such as railway and highway embankments, road and rail subgrades, dams for water resources storage, embankments for flood protection and foundation for buildings. One way to improve their performance is to reinforce the soil by introducing tension-resisting elements. Multiphase materials provide a high degree of flexibility in design with potential for cost and energy efficiency. Traditional methods of earth reinforcement use a large variety of continuous planar synthetic inclusions such as strips, fabrics or geotextiles [1]. The inclusions are normally oriented in a preferred direction, dependent on the geometry of the structure, the nature of the applied loads and the expected tensile strains in the soil. There has been much research on this topic over the last few decades. An alternative method uses short, flexible fibres as tensile-resisting elements, randomly distributed throughout the soil mass. While the ability of fibre inclusions to improve the general soil behaviour has been demonstrated in several studies [[2–7] among others], the technology of fibre reinforcement of soils has not been decisively adopted by industry mainly because of the lack of methodical performance appraisal, which requires the following: (i) understanding of the interaction mechanism between the soil and inclusions; (ii) constitutive modelling development for design and predictive capabilities; and (iii)

*Correspondence to: Andrea Diambra, Department of Civil Engineering, University of Bristol, Bristol, U.K.
†E-mail: andrea.diambra@bristol.ac.uk

validation at real structural scale that includes development of cost-effective mechanical tools for large scale fibre/soil mixing and fabrication processes. The outcomes of the present work respond to the first two requirements.

Soil behaviour is a consequence of the particulate nature of the material. When fibres are added, the complexity is amplified by the fibre-particle scale effects [3, 8]. Particulate analogues based on discrete element modelling (DEM), with parallel treatment of soil particles and random fibres, have been developed to understand how random flexible fibres generate a bond within the soil and affect the kinematics of the particulate matrix [9, 10]. Since at the scale of typical geotechnical systems, soils are normally (and necessarily) described as continua, it is still desirable to model the fibre/soil mixture as a single material or continuum because the vehicle for their use is invariably a continuum numerical analysis program. Based on hypothesis derived directly from experimental observations, a constitutive model for fibre reinforced sand is proposed in this paper. Previous research [6, 11, 12] has demonstrated that the superposition of the effects of the sand matrix and the fibres is an efficient modelling approach for this kind of composite material. While the behaviour of the sand matrix is simulated here using the bounding surface, kinematic hardening, Severn-Trent sand model [13], the fibres are considered as mono-dimensional discrete reinforcing elements, which mobilize tensile resistance as they are pulled in the course of the interaction with the sand particles. The fibre effect is treated as a force with defined direction based on the knowledge of the fibre orientation [14, 15]. The Gauss–Ostrogradsky (or divergence) theorem is employed to define the continuum equivalent of the discrete forces in the fibres so that the desired continuum constitutive model for the fibre-reinforced sands can be developed. The use of a density-dependent model for the sand allows the introduction of an additional fibre densification effect of the sand matrix, and this turns out to be fundamental for the understanding of the volumetric behaviour of fibre-reinforced soils. Such a mechanism provides a direct route to the reproduction of the undrained behaviour of fibre-reinforced sand [16]. A new concept for capturing the failure of the composite material is also proposed. The constitutive model is formulated here for axi-symmetric triaxial conditions and then is challenged for the compression and extension triaxial loading for sand reinforced with three different types of fibres. It will also be shown that the model can effectively be employed as a tool to explore the complexities of the internal fibre/sand interaction mechanisms.

2. NOTATION

The notation used for stresses and strain quantities for the composite material as well as for its constituents (the sand matrix and the fibres) is summarized in Table I. Note that effective stress in the composite material are indicated with $\boldsymbol{\sigma}^* = [p^*,\ q^*]^{\mathrm{T}}$, where p^* is the effective mean stress defined as $p^* = p\text{-}u$ where u is the pore water pressure, whereas q^* is the deviator stress of the composite, which, although unaffected by pore water pressure, is denoted with '*' for uniformity of notation. The conventional dash symbol $\boldsymbol{\sigma}' = [p',\ q']^{\mathrm{T}}$ is used for the effective stress in the sand matrix. The overbar symbol denotes equivalent average quantities calculated for the fibre phase $\left(\overline{\boldsymbol{\sigma}}_{\mathbf{f}} = \left[\bar{p}_f, \bar{q}_f\right]^T \text{ and } \overline{\boldsymbol{\varepsilon}}_{\mathbf{f}} = \left[\bar{\varepsilon}_{fp}, \bar{\varepsilon}_{fq}\right]^T\right)$, which should not be confused with the axial stress (σ_f) and axial strain (ε_f) in the individual fibre. Compressive stresses and strains are assumed positive. Bold symbols indicate tensor quantities.

Table I. Summary of stresses and strains notation adopted in this paper.

	Stresses		
	Total	Effective	Strains
Composite	$\boldsymbol{\sigma} = [p,\ q]^{\mathrm{T}}$	$\boldsymbol{\sigma}^* = [p^*,\ q^*]^{\mathrm{T}}$	$\boldsymbol{\varepsilon} = [\varepsilon_p,\ _q]^{\mathrm{T}}$
Sand matrix	—	$\boldsymbol{\sigma}' = [p',\ q']^{\mathrm{T}}$	$\boldsymbol{\varepsilon}_{\mathbf{m}} = [\varepsilon_{mp},\ _{mq}]^{\mathrm{T}}$
Fibres (average)	—	$\boldsymbol{\sigma}_{\mathbf{f}} = \left[\bar{p}_f, \bar{q}_f\right]^T$	$\overline{\boldsymbol{\varepsilon}}_{\mathbf{f}} = \left[\bar{\varepsilon}_{fp}, \bar{\varepsilon}_{fq}\right]^T$

DOI: 10.1002/nag

3. EXPERIMENTAL BEHAVIOUR OF FIBRE-REINFORCED SANDS

3.1. Materials, sample preparation and testing programme

Diambra *et al*. (2010) [6] performed an extensive triaxial experimental campaign to investigate the reinforcing effect of crimped polypropylene fibres (named fibre type 1 in this paper) when mixed with Hostun sand. The mechanical behaviour of the fibre reinforced material was investigated for both triaxial compression and extension over a large range of confining stresses and sand densities. This initial experimental campaign has been extended using the same sand but other two types of polypropylene fibres with different stiffness, strength and geometric properties. These fibres will be called here monofilament fibres (type 2) and platy fibres (type 3). A picture of three fibres is reported in Figure 1, whereas a summary of the physical properties of the fibres and the Hostun RF sand is given in Table II.

Cylindrical samples of 70-mm height and 70-mm diameter were prepared in three layers of equal height using the moist tamping technique. Ang and Loehr (2003) [17] state that specimens of approximately 70 mm in diameter or greater are reasonably representative of the 'mass' properties of fibre-reinforced soils for fibres up to 50-mm length. Furthermore, Ibraim *et al*. (2012) [18] showed that the sample layering associated with the moist tamping fabrication procedure appears to have a limited effect on the fibre orientation distribution for all the type of fibres used in this study.

The drained triaxial compression and extension tests were conducted on fully saturated, isotropically consolidated specimens. Detailed description of the sample preparation procedure and testing conditions are given in Diambra *et al*. (2010) [6] and Ibraim *et al*. (2012) [18]. The quantity of fibres added to the sand was defined as a proportion of dry weight of sand (w_f):

$$w_f = \frac{W_f}{W_s} \tag{1}$$

where W_f is the weight of fibres and W_s is the dry weight of sand.

The tests performed in this research and those by Diambra *et al*. (2010) [6] are all reported in Table III. Information given in Table III considers loading mode (C for compression and E for extension), confining pressure (σ_r^*), void ratios at the end of the consolidation stage (e_c) and fibre content (w_f). It should be noted that comparison between unreinforced and reinforced samples has been made by keeping unchanged the initial sample fabrication volume, the quantity of sand W_s, and by adding different proportions of fibres. The void ratio for reinforced specimens considers fibres as part of solids.

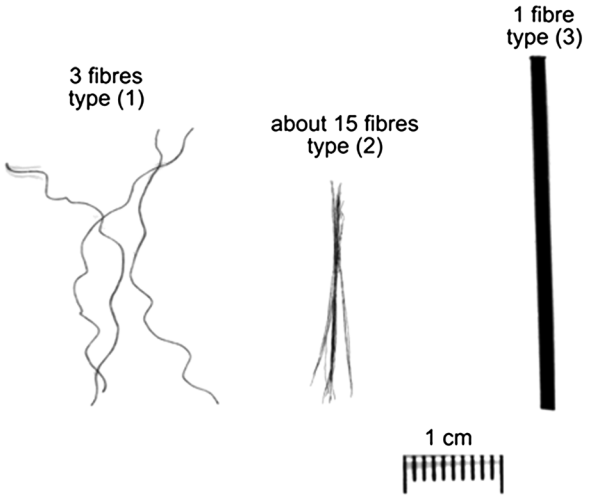

Figure 1. Fibres analysed in this paper.

DOI: 10.1002/nag

Table II. Characteristics of the sand and fibres used in the experimental investigation.

HOSTUN RF SAND

Siliceous amount	Grain shape	Mean grain size D_{50}	Coefficient of uniformity $C_u = (D_{60}/ D_{10})$	Coefficient of gradation $C_g = (D_{30})^2/(D_{60}\, D_{10})$	Specific gravity G_s	Max and min voids ratio $(e_{max} \div e_{min})$
$SiO_2 > 98\%$	Angular to sub-angular	0.32 mm	1.70	1.1	2.65	1.000 ÷ 0.630

FIBRES

Fibre type	Fibre name	Specific gravity G_f	Cross Section	Length (mm)	Aspect ratio	Tensile strength (MPa)	Elongation at break
(1)	Crimped fibres	0.91	Circular diameter 0.1 mm	35	350	22.5	160%
(2)	Monofilament fibres	0.91	Circular diameter 0.03 mm	20	667	58.0	—
(3)	Platy fibres	0.91	Linear 0.12 × 1.45 mm	40	85	—	—

DOI: 10.1002/nag

Table III. Summary of experimental tests.

Specimens reinforced with fibre type 1							
Test name	Test type C/E	σ^*_r (kPa)	e_c	w_f(%)	q^*/p^*_{serv}	q^*/p^*_{fail}	ψ_{max} (°)
L030-00-D	C	30	1.000	0	1.44	—	2.5
L030-03-D-1	C	30	0.982	0.3	2.01	—	1.5
L030-06-D-1	C	30	0.957	0.6	2.34	—	3.5
L030-09-D-1	C	30	0.955	0.9	2.56	—	3.0
L060-00-D	C	60	0.999	0	1.39	—	1.8
L060-03-D-1	C	60	0.991	0.3	1.83	—	2.0
L060-06-D-1	C	60	0.969	0.6	2.15	—	2.4
L060-09-D-1	C	60	0.948	0.9	2.35	—	4.5
L100-00-D	C	100	0.991	0	1.36	—	1.5
L100-03-D-1	C	100	0.966	0.3	1.74	—	0.5
L100-06-D-1	C	100	0.945	0.6	1.98	—	2.0
L100-09-D-1	C	100	0.936	0.9	2.26	—	2.1
L200-00-D	C	200	0.980	0	1.33	—	1.0
L200-03-D-1	C	200	0.948	0.3	1.59	—	0.6
L200-06-D-1	C	200	0.935	0.6	1.81	—	0.7
L200-09-D-1	C	200	0.912	0.9	2.02	—	—
M030-00-D	C	30	0.915	0	1.52	—	7.0
M030-03-D-1	C	30	0.885	0.3	2.09	—	9.4
M030-06-D-1	C	30	0.873	0.6	2.48	—	10.4
M100-00-D	C	100	0.914	0	1.44	—	3.5
M100-03-D-1	C	100	0.895	0.3	1.78	—	4.5
M100-06-D-1	C	100	0.886	0.6	2.05	—	6.0
M200-00-D	C	200	0.915	0	1.36	—	2.1
M200-03-D-1	C	200	0.902	0.3	1.62	—	3.5
M200-06-D-1	C	200	0.874	0.6	1.88	—	4.4
M300-00-D	C	300	0.928	0	1.32	—	1.1
M300-03-D-1	C	300	0.899	0.3	1.53	—	2.0
M300-06-D-1	C	300	0.895	0.6	1.77	—	3.5
D030-00-D	C	30	0.804	0	1.6	—	23.5
D030-03-D-1	C	30	0.802	0.3	2.24	—	21.5
D100-00-D	C	100	0.803	0	1.47	—	16.0
D100-03-D-1	C	100	0.800	0.3	1.95	—	17.1
D200-00-D	C	200	0.798	0	1.46	—	11.2
D200-03-D-1	C	200	0.780	0.3	1.76	—	14.4
Test name	Test type C/E	σ^*r (kPa)	e_c	w_f(%)	q^*/p^*_{serv}	q^*/p^*_{fail}	ψ_{max} (°)
EL100-00-D	E	100	0.989	0	—	−0.97	4.0
EL100-03-D-1	E	100	0.948	0.3	—	−1.03	4.5
EL100-06-D-1	E	100	0.928	0.6	—	−1.09	6.8
EL200-00-D	E	200	0.957	0	—	−0.95	2.2
EL200-03-D-1	E	200	0.934	0.3	—	−0.98	4.1
EL200-06-D-1	E	200	0.908	0.6	—	−1.03	6.0
EM100-00-D	E	100	0.874	0	—	−1.00	6.3
EM100-03-D-1	E	100	0.862	0.3	—	−1.06	8.8
EM100-06-D-1	E	100	0.843	0.6	—	−1.14	13.8
ED100-00-D	E	100	0.798	0	—	−1.09	12.6
ED100-03-D-1	E	100	0.776	0.3	—	−1.13	17.2
Specimens reinforced with fibre type 2							
Test name	Test type C/E	σ^*_r (kPa)	e_c	w_f(%)	q^*/p^*_{serv}	q^*/p^*_{fail}	ψ_{max} (°)
L030-00-D	C	30	1.000	0	1.44	1.46	2.5
L030-03-D-2	C	30	0.987	0.3	2.45	2.59	0.8
L030-045-D-2	C	30	0.976	0.45	2.59	2.69	1.8
L030-06-D-2	C	30	0.971	0.6	2.66	2.76	2.3
L060-00-D	C	60	0.999	0	1.39	1.45	1.8
L060-03-D-2	C	60	0.985	0.3	2.24	2.39	0.9
L060-045-D-2	C	60	0.975	0.45	2.35	2.52	0.8
L060-06-D-2	C	60	0.961	0.6	2.5	2.6	1.2
L100-00-D	C	100	0.991	0	1.36	1.42	1.5

(Continues)

DOI: 10.1002/nag

Table III. Continued

Specimens reinforced with fibre type 2							
Test name	Test type C/E	σ^*_r (kPa)	e_c	w_f(%)	q^*/p^*_{serv}	q^*/p^*_{fail}	ψ_{max} (°)
L100-03-D-2	C	100	0.964	0.3	2.01	2.17	1.3
L100-045-D-2	C	100	0.960	0.45	2.24	2.35	1.3
L100-06-D-2	C	100	0.946	0.6	2.35	—	—
M100-00-D	C	100	0.914	0	1.44	1.48	3.5
M100-03-D-2	C	100	0.883	0.3	2.14	2.17	6.5
M100-045-D-2	C	100	0.875	0.45	2.33	2.37	7.2
EL100-00-D	E	100	0.989	0	—	−0.97	4.0
EL100-03-D-2	E	100	0.968	0.3	—	−0.986	11.8
EL100-06-D-2	E	100	0.940	0.6	—	−1.084	23.7
Specimens reinforced with fibre type 3							
Test name	Test type C/E	σ^*r (kPa)	e_c	w_f(%)	q^*/p^*_{serv}	q^*/p^*_{fail}	ψ_{max} (°)
L030-00-D	C	30	1.000	0	1.44	1.46	2.5
L030-03-D-3	C	30	0.986	0.3	1.81	1.89	1.9
L030-06-D-3	C	30	0.977	0.6	2.09	2.17	2.3
L030-09-D-3	C	30	0.961	0.9	2.28	2.35	2.4
L060-00-D	C	60	0.999	0	1.39	1.45	1.8
L060-03-D-3	C	60	0.978	0.3	1.69	1.74	1.6
L060-06-D-3	C	60	0.966	0.6	1.99	2.10	1.5
L060-09-D-3	C	60	0.951	0.9	2.31	2.41	1.0
L100-00-D	C	100	0.991	0	1.36	1.42	1.5
L100-03-D-3	C	100	0.980	0.3	1.64	1.74	1.0
L100-06-D-3	C	100	0.956	0.6	1.98	2.05	0.1
L100-09-D-3	C	100	0.946	0.9	2.25	—	0.4
M100-00-D	C	100	0.914	0	1.44	1.48	3.5
M100-03-D-3	C	100	0.880	0.3	1.73	1.76	5.0
M100-06-D-3	C	100	0.864	0.6	2.02	2.08	4.4
EL100-00-D	E	100	0.989	0	—	−0.97	4.0
EL100-03-D-3	E	100	0.988	0.3	—	−0.98	18.4
EL100-06-D-3	E	100	0.986	0.6	—	−0.99	17.4

It is worth noticing that the tests have been grouped according to the nominal relative density, D_r ($D_r = (e_{max} - e)/(e_{max} - e_{min})$), of the unreinforced specimens. Three nominal fabrication densities have been chosen, very loose ($D_r \approx 0\,\%$), loose ($D_r \approx 25\,\%$) and medium dense ($D_r \approx 50\,\%$), which will be called in the following of this paper test series *(L)*, series *(M)* and series *(D)*, respectively. Notice that the letters *L*, *M* and *D* can be also found in the given test name. Because the maximum amount of fibres that can be added decreases with the sample relative density [19], to allow a reasonable range of fibre contents, samples on the loose side of the relative density spectrum have been investigated here.

3.2. Experimental results

The main experimental results are summarized in Table III. For compressive loading, because the proper failure of the reinforced samples was observed only at very large strains for fibres (2) and (3) while was not even reached for fibres type (1) (see Figure 2 a, c, e), a serviceability failure criterion was introduced at 20% axial strain. Thus in Table III, the deviatoric stress ratios at the serviceability failure (q^*/p^*_{serv}) and at proper failure (q^*/p^*_{fail}) are both reported for the compressive loading while only that at failure is shown for the extension case. The observed maximum angle of dilatancy (ψ_{max}) is also indicated in the Table III. The mobilized angle of dilatancy for triaxial conditions is defined here as the inverse tangent of the ratio of incremental volumetric and axial strains, and for simplicity it has been assumed that the elastic components of the strain increments are small compared with the plastic components (denoted with the superscript ^{p}), to give:

DOI: 10.1002/nag

$$\tan\psi = -\frac{\dot{\varepsilon}_p^p}{\left|\dot{\varepsilon}_a^p\right|} \approx -\frac{\dot{\varepsilon}_p}{\left|\dot{\varepsilon}_a\right|} \tag{2}$$

The observed stress strain behaviour over the range of stress, density and fibre content confirms previous findings on the behaviour of fibre reinforced soils. The effectiveness of the reinforcement is influenced by fibre properties including type, volume fraction, length, aspect ratio, modulus of elasticity, orientation characteristics including particle size, shape and gradation, as well as stress level and density (e.g. [5, 20]). The typical triaxial behaviour for both unreinforced and reinforced specimens (for all three types of fibres) is shown in Figure 2 in terms of variations of effective deviatoric stress (q^*) and volumetric strain (ε_p) with deviatoric strain (ε_q). These compression and extension tests were performed on very loose samples (nominal relative density $D_r \sim 0\%$) with an effective consolidation pressure (p^*_c) of 100 kPa.

The primary attributes for the construction of proposed constitutive model have been set from the following experimental observations:

O.1 **Fibre content**. For triaxial compression conditions, the increased mobilized strength induced by the addition of fibres is remarkable and highly dependent on the fibre content (Figure 2a, c, e).

O.2 **Strain level dependency**. Heineck *et al*. (2005) [21] suggest that the initial stiffness of the composite soil is not influenced by the presence of fibres, in other words, over the small strain domain the behaviour of the composite is solely governed by the sand matrix. However, Figure 2 shows that the behaviour of the three types of reinforced samples in compression diverges from the unreinforced one as the tests proceed. The fibre/sand interaction mechanism is strain level dependent.

O.3 **Bonding effect**. For fibre type (1), although some tests were taken to 40% axial strain, the reinforced specimens show a somehow bilinear stress–strain relationship without any sign of failure of bonding between fibres and sand grains. Careful observation of exhumed samples showed no sign of visible plastic straining of the fibres. This suggests that, although the bonding between fibres and sand is fully active, some partial relative slippage may still occur.

O.4 **Pull-out mechanism**. The monofilament and platy fibres (types 2 and 3) show a flattening of the deviatoric stress-axial strain curve, which indicates attainment of a failure state for the reinforced sample. Observation of exhumed samples showed no sign of breakage or visible plastic straining of these two fibres. This suggests that at large strains, the bonding between fibres and sand can be lost, and complete pullout of the fibres occurs.

O.5 **Fibre orientation**. There is negligible increase in mobilized strength in triaxial extension. Diambra *et al*. (2010) [6] demonstrated that the preferred horizontal bedding of fibres induced by the moist tamping technique [14] can be considered responsible for this anisotropic response.

O.6 **Volumetric effect**. On the volumetric plane (Figure 2b, d, f), the contractive behaviour of the unreinforced sample becomes more dilative when fibres (all three types) are added for both compression and extension conditions. The decrease in void ratio due to the fibre addition is typically well below 0.05, and this change in the density can only partially explain the increased dilation observed for the composite material. Furthermore, it may be expected that the pronounced tensile contribution of the fibres would provide increased matrix confinement and in turn a more contractive response. Thus, an additional fibre/sand interaction mechanism effect should be further considered to explain the experimentally observed increased dilation.

4. MODELLING FRAMEWORK

4.1. Modelling hypotheses

The behaviour of fibre-reinforced soil is determined by superposing the contribution of the fibres and the behaviour of plain sand. The sand matrix obeys its own constitutive rule and is described using the

DOI: 10.1002/nag

Severn-Trent sand model [13]. The contribution of fibres is estimated through the following hypotheses, which have been directly suggested by the previous experimental observations:

H.1: Fibres are homogeneously distributed throughout the sand matrix. The stress and strain states of the composite material are derived from a volumetric averaging procedure of the stress and strain states of the constituents (suggested by O.1, and developed in Section 4.3).
H.2: Fibres are considered as mono-dimensional, discrete (not continuum), elastic elements with only tensile resistance mobilized by the tensile strains developed in the reinforced soil (suggested by O.2, and developed in Section 6.2).
H.3: Partial relative slippage between the fibres and the sand grains occurs during loading (suggested by O.3 and developed in Section 6.3).
H.4: Fibres can pull-out of the sand matrix (suggested by O.4, and developed in Section 6.4).
H.5: Fibres are considered along with their orientation (suggested by O.5, and developed in Section 6.1).
H.6: The presence of fibres affects the packing of the sand matrix (suggested by O.6, and developed in Section 4.2).

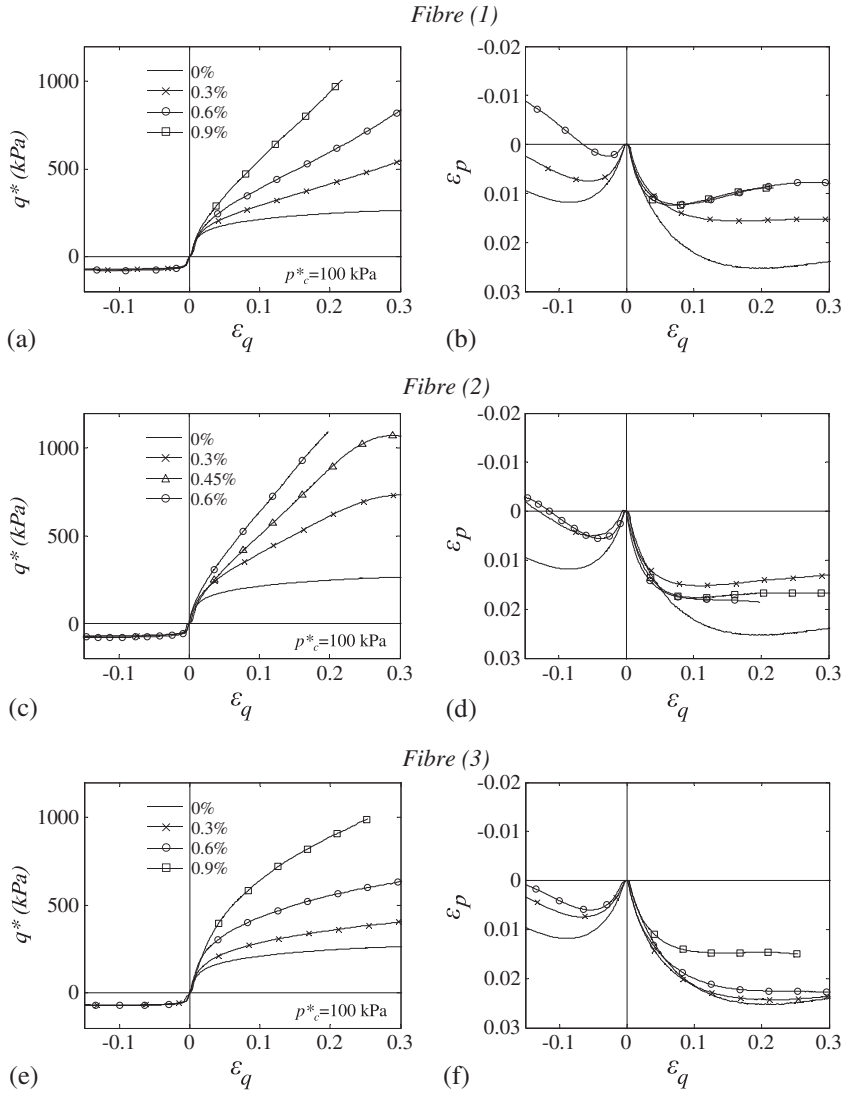

Figure 2. Deviator stress–shear strain and volumetric strain–shear strain response for drained compression and extension triaxial tests on series *(L)* unreinforced and reinforced samples, isotropically consolidated at $p^*_c = 100$ kPa (legend gives the fibre content w_f).

DOI: 10.1002/nag

4.2. Phase relationships (H.6)

The total volume of an unreinforced specimen (V) is made up of sand matrix (V_s) and voids (V_v); the phase diagram is schematically shown in Figure 3a. For samples reinforced with fibres, the volume of solids occupied by the fibres (V_f) needs to be included in the diagram as shown in Figure 3b. However, as anticipated by the modelling hypothesis H.6, the total volume of the voids (V_v) can be divided in two parts 'attached', respectively, to the sand matrix (V_{vs}) and to the fibres (V_{vf}) (Figure 3c). Considering the phase diagram in Figure 3c, it is possible to define specific volumes for the fibre-reinforced specimen (υ), sand matrix (υ_m) and fibres (υ_f):

$$\upsilon = \frac{V}{V_s + V_f} \quad \upsilon_m = \frac{V_{vs} + V_s}{V_s} \quad \upsilon_f = \frac{V_{vf} + V_f}{V_f} \tag{3}$$

and the relationships between the specific volume and volumetric strain for each phase are as follows:

$$\dot{\varepsilon}_p = -\frac{\dot{\upsilon}}{\upsilon} \quad \dot{\varepsilon}_{mp} = -\frac{\dot{\upsilon}_m}{\upsilon_m} \quad \dot{\varepsilon}_{fp} = -\frac{\dot{\upsilon}_f}{\upsilon_f} \tag{4}$$

Manipulation of (3) leads to a relation between the specific volumes of the composite material and of the constituents:

$$\upsilon = \frac{1}{1 + \rho_f}\left(\upsilon_m + \upsilon_f \rho_f\right) \tag{5}$$

For a fixed specific volume of the composite, any 'attachment' of voids to the fibres (i.e. $\upsilon_f > 1$) results in a decreased value of the specific volume for the sand matrix—a densification of the sand matrix induced by the presence of fibres.

The definition of the volumetric concentration of the two constituents must account for both the volumes of solids and voids to be expressed as follows:

$$\mu_m = \frac{(V_s + V_{vs})}{V} = \frac{V_s}{V}\upsilon_s \quad \mu_f = \frac{\left(V_f + V_{vf}\right)}{V} = \frac{V_f}{V}\upsilon_f \tag{6}$$

and their sum is equal to unity by definition.

4.3. Combination of sand and fibres (H.1)

4.3.1. The stress state of the composite. The determination of the composite stress state requires the combination of different stress states in the fibres and the soil. The sand matrix is considered here as a continuum and it is supposed that the local stress state is homogeneous throughout its volume being equal to the average value $\boldsymbol{\sigma}$'. Fibres are unidimensional discrete elements, but the assumed smearing of fibre orientations is continuous so that within a representative element, there is a single average equivalent stress state $\overline{\boldsymbol{\sigma}}_f$. The procedure for the derivation of this average stress will be described in Section 5.1.3. By using a volumetric averaging approach, the stress state of the composite can be derived from those of its constituents by the following:

$$\boldsymbol{\sigma}^* = \mu_m \boldsymbol{\sigma}' + \mu_f \overline{\boldsymbol{\sigma}}_f \tag{7}$$

and its incremental form is as follows:

$$\dot{\boldsymbol{\sigma}}^* = \mu_m \dot{\boldsymbol{\sigma}}' + \dot{\mu}_m \boldsymbol{\sigma}' + \mu_f \dot{\overline{\boldsymbol{\sigma}}}_f + \dot{\mu}_f \overline{\boldsymbol{\sigma}}_f \tag{8}$$

4.3.2. The strain state of the composite. Manipulation of the definitions of incremental volumetric strains for the composite, and each constituent phase in (6) leads to the incremental relationship

DOI: 10.1002/nag

between the incremental volumetric strains of the composite $\left(\dot{\varepsilon}_p\right)$ and its constituents $\left(\dot{\varepsilon}_{mp}, \dot{\bar{\varepsilon}}_{fp}\right)$:

$$\dot{\varepsilon}_p = \dot{\varepsilon}_{mp}\mu_m + \dot{\bar{\varepsilon}}_{fp}\mu_f \tag{9}$$

Consistently with (9), the relationship between the incremental tensor of strains of the composite and its constituents can be defined as follows:

$$\dot{\boldsymbol{\varepsilon}} = \dot{\boldsymbol{\varepsilon}}_{\mathbf{m}}\mu_m + \dot{\bar{\boldsymbol{\varepsilon}}}_{\mathbf{f}}\mu_f \tag{10}$$

As generally assumed for soils, it is supposed that any deformation of the solid fraction of the fibres and of the soil particles themselves is negligible. There is no reliable experimental evidence to support or conflict with an assumption that the volume of the voids 'attached' to the fibres remains constant during the loading process. Thus, it is assumed that the overall deformation undergone by the fibre phase (solids and voids) during loading is negligible compared with that undergone by the sand matrix $\left(\bar{\varepsilon}_f \approx 0\right)$. Therefore, the specific volume of the fibres (υ_f) is constant, and it will be assumed to be an input model parameter. Equation (10) can then be simplified:

$$\dot{\boldsymbol{\varepsilon}} = \dot{\boldsymbol{\varepsilon}}_{\mathbf{m}}\mu_m \tag{11}$$

5. CONSTITUTIVE MODEL FOR SAND MATRIX

Severn-Trent sand [13] is a bounding surface, kinematic hardening soil model. The strength surface is the bounding surface, and it always encloses the yield surface (Figure 4), which bounds a purely elastic region. The actual stress state may lie on or inside the yield surface. Both the strength and yield surfaces are wedges in the *q'-p'* plane with their apexes coincident with the origin of the plane. The model assumes a non-associative flow rule and its form is a modification of the original Cam-Clay model [22]. The size of the strength surface is not constant but depends on the current value of a state parameter [23], which describes the volumetric distance from the locus of ultimate critical states. For soils which are looser than the critical state, the current strength is lower than the critical state strength; for soils which are denser than the critical state the current strength is higher than the critical state strength. The flow rule ensures that shearing at stress ratios below or above the critical state stress ratio produces plastic volumetric compression (densification) or expansion (dilation) so that shearing automatically steers the sand towards the critical state—although this ultimate strength can only be theoretically reached after infinite shear strain. The model requires 10 parameters, which are listed and calibrated in Section 8.1.1.

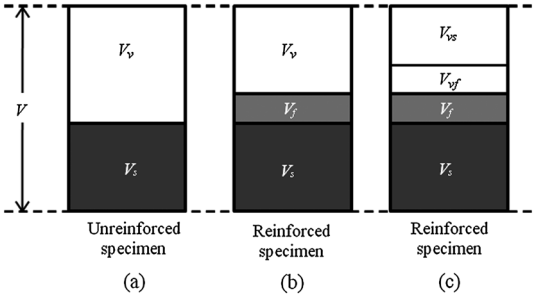

Figure 3. Phase diagrams for (a) unreinforced specimen, (b) reinforced specimen without partition of volume of voids and (c) reinforced specimen with partition of volume of voids.

DOI: 10.1002/nag

6. CONSTITUTIVE MODEL FOR FIBRES

6.1. Orientation of fibres (H.5)

For the definition of the distribution of fibre orientation, we can introduce the spherical coordinates in Figure 5, where θ is elevation angle measured from the horizontal reference plane, whereas α is the azimuth angle measured on the horizontal plane from the generic direction x. The function $\rho_{\theta\alpha} = \rho_{\theta\alpha}(\theta,\alpha)$ indicates the probability that fibres will be found oriented within the infinitesimal domain $d\theta d\alpha$ represented in Figure 5. By definition, the integral of the probability function $\rho_{\theta\alpha}$ must satisfy the following constraint:

$$\int_0^{\pi} \int_{-\pi/2}^{\pi/2} \rho_{\theta\alpha} \cos(\theta) d\theta d\alpha = 1 \tag{12}$$

where the *cos(θ)* term is introduced because of the spherical coordinate system assumed. For isotropic orientation of fibres, the function $\rho_{\theta\alpha}$ assumes a constant value equal to $1/2\pi$. In the following, other forms of the function $\rho_{\theta\alpha}$ will be introduced and (12) will be satisfied for any of the forms assumed.

For a reinforced sample with a total number of fibres N, the number of fibres oriented within the infinitesimal domain $d\theta d\alpha$ (Figure 5) is $N\rho_{\theta\alpha}$. The number of fibres oriented at (θ,α) per unit volume of fibre space (volume of fibres plus volume of attached voids) $\bar{N}_{\theta\alpha}$is as follows:

$$\bar{N}_{\theta\alpha} = \bar{N}\rho_{\theta\alpha} = \frac{1}{a_f l_f \upsilon_f} \rho_{\theta\alpha} \tag{13}$$

where $\bar{N}$ is the number of fibres per unit volume of fibre space, a_f is the cross-sectional area of the fibres and l_f is the length of the fibres.

6.2. Stress–strain response of the single fibre (H.2)

The fibres are unidimensional elements, which can react only to tension, with negligible compressive and bending stiffness. Assuming that they respond elastically, the tensile stress–strain (σ_f - ε_f) relationship for the individual fibre is as follows:

$$\sigma_f = E_f \langle \varepsilon_f \rangle \tag{14}$$

where E_f is Young's modulus for the fibre material, and the symbol $\langle\rangle$ indicates a modified form of the Macaulay brackets for which

$$\langle \varepsilon_f \rangle = \begin{cases} \varepsilon_f \text{ for } \varepsilon_f < 0 \\ 0 \text{ for } \varepsilon_f \geq 0 \end{cases} \tag{15}$$

because tensile strains are assumed negative.

The post-test analysis of the reinforced samples tested in parallel experimental research suggested that fibre pullout occurred before the fibres could reach their plastic threshold and eventually break [24]. Thus, there is no need to incorporate any limit to the tensile stresses mobilized in the fibres resulting in either snapping of fibres or a transition to perfectly plastic stretching. This assumption greatly simplifies the modelling of the fibres without jeopardizing the quality of the simulations.

6.3. Bonding between sand and fibres (H.3)

Although the strains in the fibres follow the deformation pattern of the reinforced soil, the bonding between the fibres and sand grains may not be perfect, and some slippage may occur between the two phases. A modifying factor f_b measures the local 'degree of slip' along the fibre surface as previously introduced by Machado *et al*. (2002) [25]. Although alternative expressions for the factor f_b can be adopted, this factor is assumed here to be exponentially dependent on the value of the mean effective stress of the soil matrix as also suggested in Diambra *et al*. (2010) [6], leading to the

DOI: 10.1002/nag

relation of fibre strain (ε_f) to the strain of the reinforced soil (ε) along the direction of the fibre:

$$f_b = \frac{\dot{\varepsilon}_f}{\dot{\varepsilon}} = K_e \left(1 - \exp\left(-\frac{p'}{p_{ref}}\right)\right) \tag{16}$$

where p_{ref} takes the value of 100 kPa. K_e is a coefficient which determines the maximum allowable value for f_b and can be thought as an efficiency factor of the contact between the fibres and the sand matrix. It can vary from 0 to 1 (as does f_b). In the absence of confining stress there is total slippage between fibres and surrounding grains ($f_b = 0$).

6.4. Fibre pullout (H.4)

Pullout is the typical mechanism governing the failure of fibre-reinforced samples below the critical confining stress [26]. For higher confining stresses, attainment of the plastic limit and/or breakage of the fibres may be more probable factors influencing failure of the reinforced material [[27, 28] among others]. Given the nature of the experimental results to be simulated, these last failure mechanisms have not been considered, although they would require only minor modification of the assumed stress–strain relationship for the single fibre.

Pullout is considered to take place when the mobilized shear resistance at the fibre–sand interface has reached its maximum allowable value τ_{sf}^L [28]:

$$\tau_{sf}^L = a_{sf} + \sigma^*_{n,ave} \tan\delta_{sf} \tag{17}$$

where a_{sf} is the adhesive component of the interface shear strength between the soil and the fibres, tan δ_{sf} is the frictional component and $\sigma^*_{n,ave}$ is the average normal stress acting on the fibres which is simplistically assumed equal to p^* in this work. Considering a uniform distribution of shear stress along the fibre surface, it is possible to calculate the limit stress mobilized in the fibres σ_f^L through the equilibrium of the forces:

$$\sigma_f^L = \frac{p_f l_f}{2a_f}\left(a_{sf} + p^* \tan\delta_{sf}\right) \tag{18}$$

where a_f, p_f and l_f are the cross-sectional area, cross sectional perimeter and length of the fibres, respectively. Thus, it is assumed that when stress in a fibre reaches the threshold stress σ_f^L, it pulls out, and its incremental contribution to the overall stress becomes null.

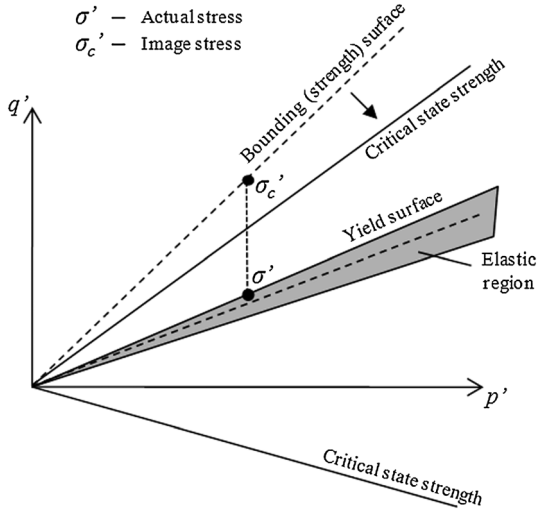

Figure 4. Schematic view of the strength surface and elastic region for the Severn-Trent sand model [13].

DOI: 10.1002/nag

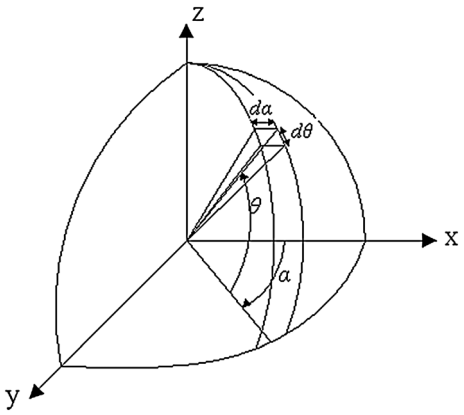

Figure 5. Spherical coordinates used for the definition of the fibre orientation distribution.

6.5. *Overall contribution of the fibres*

The fibre is contributing with a force (or stress over the cross-sectional area) dependent on its orientation. The agglomerate of independent fibres is not a continuum: their contribution to the overall stress state is through the definition of an equivalent stress using the spherical integration space defined in Figure 5. All fibres have been imagined as moved to have their mid-point coincident with the origin of the sphere while retaining their orientation.

If the force mobilized in the fibres is thought of as being generated at the ends of the fibres, it is equivalent to tensile forces applied on the surface of the spherical integration space. Then, from the Gauss-Ostrogradsky theorem, the components of the average stress tensor $\boldsymbol{\sigma}_{\mathbf{f}ij}$ over the integration volume are linked to the tractions (t) on the surface by the following relationship:

$$\bar{\boldsymbol{\sigma}}_{\mathbf{f}ij} = \frac{1}{V}\iiint_V \boldsymbol{\sigma}_{\mathbf{f}ij}\, dV = \frac{1}{V}\iint_S x_i t_j dS \tag{19}$$

where the subscripts 'i' and 'j' refer to one of the three components in a Cartesian reference system (x, y, z), V is the volume of the integration space, S is its surface, x_i is the component along the direction i of the position x on the surface S.

The size of the integration sphere influences the distance of the application of the force (x) from the centre of the integration space and in turn affects the average stress state of the system. If uniformity of strain along the length of the fibres is assumed, it is equivalent to the fibre being pulled at its end by a force $F = \sigma_f a_f$, and the sphere must have a diameter equal to l_f. Thus, (19) can be rewritten as follows:

$$\bar{\boldsymbol{\sigma}}_{\mathbf{f}ij} = \frac{1}{V}\int_0^{2\pi}\int_0^{\pi} \frac{l_f}{2} n_i \sigma_{f\,\theta\alpha} a_f \bar{N}_{\theta\alpha} V n_j \cos(\theta) d\theta d\alpha \tag{20}$$

where the product $\sigma_{f\theta\alpha}\ a_f$ represents the force in the fibre with orientation (θ,α), the product $\bar{N}_{\theta\alpha}V$ represents the number of fibres oriented at (θ,α), and n_i and n_j represent the components along the directions i and j of the unit vector $\mathbf{n}$ normal to the sphere at (θ,α), and they reduce to simple trigonometric functions.

Considering axi-symmetric triaxial conditions and substituting (13), (14) and (16) in (20), the following incremental relationships for the vertical (axial, indicated by the subscript '$_a$') and horizontal (radial, indicated by the subscript '$_r$') stresses are derived:

DOI: 10.1002/nag

$$\dot{\bar{\sigma}}_{f\,a} = \frac{\pi}{\upsilon_f} \int_0^{\pi} E_f f_b \langle \dot{\varepsilon}_{\theta\alpha} \rangle \rho_{\theta\alpha} \sin^2(\theta) \cos(\theta) d\theta \tag{21}$$

$$\dot{\bar{\sigma}}_{f\,r} = \frac{\pi}{2\upsilon_f} \int_0^{\pi} E_f f_b \langle \dot{\varepsilon}_{\theta\alpha} \rangle \rho_{\theta\alpha} \cos^3(\theta) d\theta \tag{22}$$

where $\dot{\varepsilon}_{\theta\alpha}$ is the incremental strain of the reinforced sample along the direction (θ,α). To simplify the solution of the integrals in (21) and (22), it has been assumed that any strain release in a stretched fibre is not coupled with any decrease of tensile stress. Although this may not be necessarily true, the assumption has very little influence for the monotonic loading conditions analysed here: the proportion of fibres subjected to this particular condition is very modest as it will be the amount of stress released.

The strain increment $\dot{\varepsilon}_{\theta\alpha}$ can be expressed in terms of its axial and radial components by using the Mohr's circle for incremental strains. For triaxial conditions, the symbol $\langle\rangle$ can also be removed if the integration is performed over the domain of tensile incremental strains to give the following relationship between average stress increments of the fibre phase and composite strain increments:

$$\begin{bmatrix} \dot{\bar{\sigma}}_{fa} \\ \dot{\bar{\sigma}}_{fr} \end{bmatrix} = E_f \frac{\pi}{\upsilon_f} f \begin{bmatrix} 2\int_{l_1}^{l_2} \rho(\theta)\sin^4(\theta)\cos(\theta)\mathrm{d}\theta & 2\int_{l_1}^{l_2} \rho(\theta)\cos^3(\theta)\sin^2(\theta)\mathrm{d}\theta \\ \int_{l_1}^{l_2} \rho(\theta)\cos^3(\theta)\sin^2(\theta)\mathrm{d}\theta & \int_{l_1}^{l_2} \rho(\theta)\cos^5(\theta)\mathrm{d}\theta \end{bmatrix} f_b \begin{bmatrix} \dot{\varepsilon}_a \\ \dot{\varepsilon}_r \end{bmatrix} \tag{23}$$

where the limits l_1 and l_2 ensure that the integration is performed only over the tensile domain. Taking advantage of the symmetry of the problem in respect to the horizontal plane, $l_1 = 0$ and $l_2 = \theta_0$ for triaxial compression and $l_1 = \theta_0$ and $l_2 = \pi/2$ for triaxial extension (Figure 6a and b, respectively). θ_0 is the direction of zero incremental strains, which, according to Mohr's circle for strain increment, is

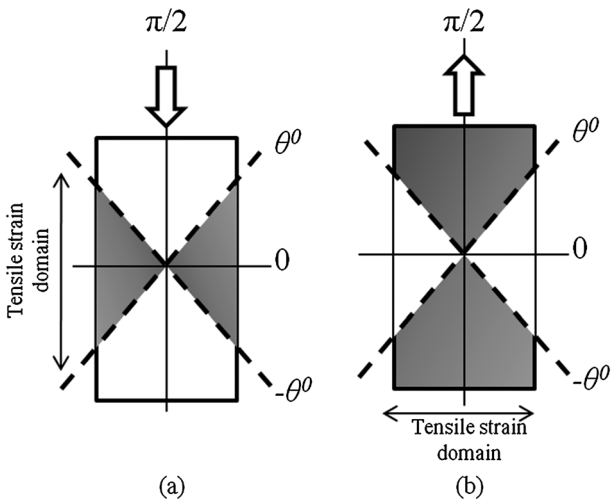

Figure 6. Domains of tensile strain orientations for compression (a) and extension (b) loadings.

DOI: 10.1002/nag

$$\theta_0 = \arctan\sqrt{-\frac{\dot{\varepsilon}_r}{\dot{\varepsilon}_a}} \tag{24}$$

For conventional triaxial p and q notation, (23) can be rewritten as

$$\begin{bmatrix} \dot{p}_f \\ \dot{q}_f \end{bmatrix} = E_f \frac{\pi}{\upsilon_f} \begin{bmatrix} M_{11} & M_{12} \\ M_{21} & M_{22} \end{bmatrix} f_b \begin{bmatrix} \dot{\varepsilon}_p \\ \dot{\varepsilon}_q \end{bmatrix} \tag{25}$$

where:

$$\left.\begin{aligned} M_{11} &= \frac{1}{9}(N_{11} + N_{12} + 2N_{21} + 2N_{22}) \\ M_{12} &= \frac{1}{3}\left(N_{11} - \frac{N_{12}}{2} + 2N_{21} - N_{22}\right) \\ M_{21} &= \frac{1}{3}(N_{11} + N_{12} - N_{21} - N_{22}) \\ M_{22} &= \frac{1}{2}(2N_{11} - N_{12} - 2N_{21} + N_{22}) \end{aligned}\right\} \tag{26}$$

and the N_{ij} terms represent the components of the matrix in (23) with the first subscript being the row number and the second subscript being the column number. The stiffness matrix of the fibre phase **[$\mathbf{M_f}$]** is defined as

$$[\mathbf{M_f}] = E_f \frac{\pi}{\upsilon_f} \begin{bmatrix} M_{11} & M_{12} \\ M_{21} & M_{22} \end{bmatrix} f_b \tag{27}$$

7. CONSTITUTIVE RELATIONSHIP FOR THE REINFORCED MATERIAL

A unique constitutive stress–strain relationship for the composite material can be defined from (8) and (11) through substitution of the stress–strain relationships defined for both fibres and sand matrix. In this process, it is useful to consider the differentiated form of (6) and its subsequent manipulation, which leads to

$$\dot{\mu}_m = (\mu_m - 1)\dot{\varepsilon}_p = -\mu_f \dot{\varepsilon}_p \quad \dot{\mu}_f = \mu_f \dot{\varepsilon}_p \tag{28}$$

The incremental stress–strain relationship for the fibre reinforced soils is

$$\begin{bmatrix} \dot{p}^* \\ \dot{q}^* \end{bmatrix} = \left\{ [\mathbf{M_m}] + \mu_f [\mathbf{M_f}] + \begin{bmatrix} p' \\ q' \end{bmatrix} \begin{bmatrix} -\mu_f \\ 0 \end{bmatrix}^T + \begin{bmatrix} \bar{p}_f \\ \bar{q}_f \end{bmatrix} \begin{bmatrix} \mu_f \\ 0 \end{bmatrix}^T \right\} \begin{bmatrix} \dot{\varepsilon}_p \\ \dot{\varepsilon}_q \end{bmatrix} \tag{29}$$

where **[$\mathbf{M_f}$]** is the stiffness matrix for the fibres in (27) and **[$\mathbf{M_m}$]** is the one for the sand matrix provided by Gajo and Muir Wood (1999) [13].

8. APPLICATION OF THE PROPOSED MODEL

8.1. Parameters calibration

8.1.1. Hostun sand. Severn-Trent sand requires two parameters to describe the elastic behaviour and eight parameters for defining the plastic behaviour of the soil. As suggested by Gajo and Muir Wood (1999) [13], Poisson's ratio was assumed equal to 0.1, and it was assumed that a scalar factor C (<1) links the shear modulus of the sand matrix G to the dynamic shear modulus G_0, which is in turn related to the specific volume υ_m and the mean effective stress p' in kPa through the relationship proposed by Hardin and Black (1966) [29]:

DOI: 10.1002/nag

$$G = C\,G_0 = C\,3230\frac{(3.97 - \upsilon_m)}{\upsilon_m}\sqrt{p'}\sqrt{p_a} \tag{30}$$

where p_a is equal to 1 kPa.

The calibration of the plastic parameters has been performed to obtain a good fit with the triaxial response of the unreinforced specimens as shown in Diambra (2010) [24]. A summary of the selected values is given in Table IV.

8.1.2. Fibres. The description of the fibres requires the definition of four parameters: the elastic modulus E_f, the fibre-sand bonding efficiency factor K_e, the fibre specific volume υ_f and the pull-out stress in the fibres σ_f^L, which is actually controlled by some constitutive parameters a_{sf} and δ_{sf}. The calibrated values for each of the three reinforcements are summarized in Table V, whereas the calibration procedure is outlined below.

- *Elastic modulus E_f*

The elastic modulus of the fibres has been chosen to fit the initial part of the tensile stress–strain behaviour of the single fibres as shown in Figure 7.

- *Fibre-sand bonding efficiency factor K_e and specific volume of fibres, υ_f*

The coefficients K_e and υ_f can be calibrated simultaneously following an iterative procedure. The coefficient K_e governs the maximum value of the 'sliding' ratio f_b between the fibres and the sand grains. The reinforcing effectiveness of the fibres, especially the slope of the stress–strain behaviour at medium-large strains, is very sensitive to the value of this parameter. If $K_e = 0$, full sliding is assumed between fibres and sand grains and the computed stress–strain behaviour of the reinforced sample is similar to that of an unreinforced one (with the exception of the densification provided by the physical presence of the fibres). If $K_e = 1$, the maximum slope of the stress–strain curve is

Table IV. Values of soil parameters for Hostun RF sand.

Parameter	Description	Value
C	Ratio of elastic shear modulus to dynamic shear modulus	0.4
v	Poisson' s ratio	0.1
φ'	Critical-state friction angle	35°
Γ	Intercept for critical-state line on υ_m- ln p' plane at p' = 1 kPa	2.08
λ	Slope of the critical-state line on υ_m- ln p' plane	0.031
k_r	Link between changes in state parameter and current strength	1.5
B	Parameter controlling hyperbolic stiffness relationship	0.0025
R	Ratio of size of yield and strength surfaces	0.1
A	Multiplier in flow rule	0.75
k_d	State parameter contribution in flow rule	1.5

Table V. Parameters adopted for the fibres.

Modelling ingredient	Description	Value		
		Fibre (1)	Fibre (2)	Fibre (3)
E_f	Elastic modulus	900 MPa	2600 MPa	4000 MPa
K_e	Sliding function $f_b = K_e\left(1 - \exp\left(-\frac{p'}{p_{ref}}\right)\right)$	0.45	0.34	0.08
υ_f	Specific volume of the fibres	3.27	4.8	2.4
σ_f^L	Limit stress for fibres $\sigma_f^L = \frac{p_f l_f}{2a_f}\left(a_{sf} + p^* \tan\delta_{sf}\right)$	-----	a_{sf} = 76 kPa δ_{sf} = 0°	a_{sf} = 4 kPa δ_{sf} = 10°

DOI: 10.1002/nag

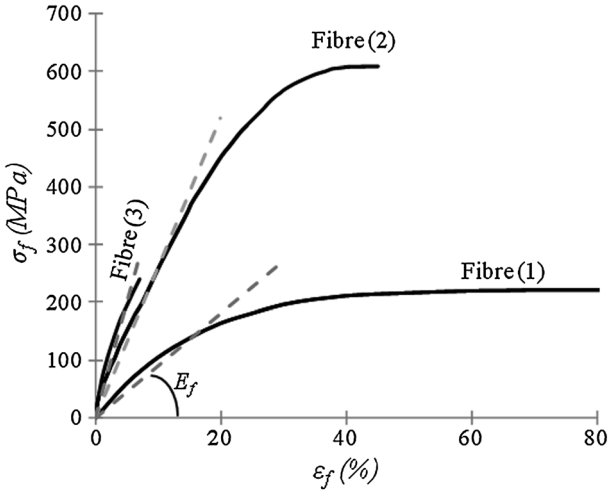

Figure 7. Average tensile stress–strain curve of 15 individual fibres and approximation with a linear elastic relationship.

achieved (Figure 8a). Thus, as first attempt of the calibration, the value of K_e can be chosen to match the stress–strain curve of the reinforced samples by taking a value of $\upsilon_f = 1$.

Because the 'attachment' of some voids to the fibre phase has been deliberately introduced to capture the increased dilation for fibre-reinforced soils, the value of υ_f can now be adjusted to match the volumetric behaviour of the selected reinforced sample (Figure 8b). This new value of υ_f may slightly change the stress–strain behaviour, so the procedure can be iterated until a good fit for both the stress–strain and volumetric behaviour is obtained as shown in Figure 8 for fibre type (1).

It is worth noticing from (23) that E_f and K_e (contained in the function f_b) are multiplicative factors of the sample strains. Therefore, if E_f of the fibres is unknown, it is possible to use the previously mentioned procedure to calibrate the product $E_f K_e$ and, thus, reduce the number of model parameters.

- *Limit stress for fibres*, σ_f^L

At failure, it can be assumed that all the fibres oriented within the tensile strain domain have mobilized the limit stress σ_f^L, whereas the mobilized stress in the fibres oriented in the compression domain is null. It is possible to link the fibre stress contribution at failure to the fibre pullout stress:

$$\bar{\sigma}_{f\,a} = \frac{\pi}{\upsilon_f} \int_0^{\theta_0} \sigma_f^L \rho_{\theta\alpha} \sin^2(\theta) d\theta = K_a \sigma_f^L \tag{31}$$

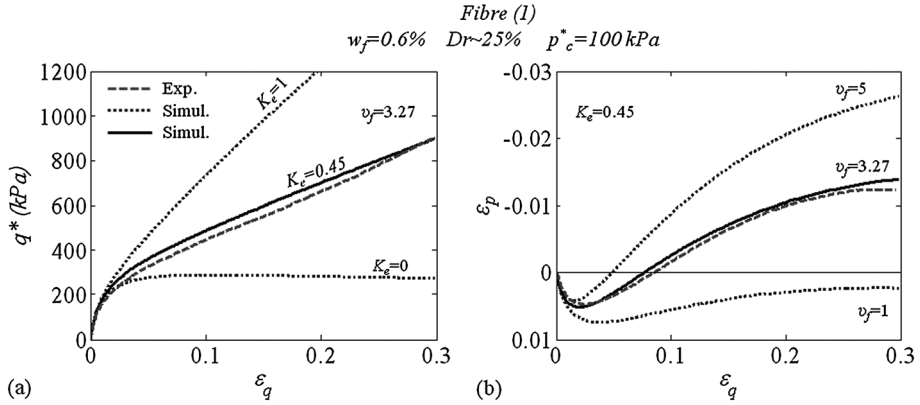

Figure 8. Procedure for determination of the fibre-sand bonding efficiency factor K_e and specific volume of fibres, υ_f.

DOI: 10.1002/nag

$$\bar{\sigma}_{f_r} = \frac{\pi}{2\upsilon_f} \int_0^{\theta_0} \sigma_f^L \rho_{\theta\alpha} \cos^2(\theta) d\theta = K_r \sigma_f^L \tag{32}$$

where the definition of the terms K_a and K_r is self explanatory and has been introduced to take advantage of the constant nature of the limit stress in the fibres σ_f^L in respect to the orientation θ. Considering that sand matrix behaves in a critical state framework and has reached the asymptotic condition of shearing without any further change in volume, the angle θ_0 is equal to the $\arctan\left(\sqrt{1/2}\right)$. At critical state, the following relationship for the stresses in the sand can be derived:

$$\sigma'_a = \sigma'_r \frac{1 + \sin\phi'}{1 - \sin\phi'} \tag{33}$$

The substitution of (31), (32) and (33) into (7) gives the next relationship between the limit stress in the fibres σ_f^L and the stress state of the reinforced soil specimens at failure:

$$\sigma_f^L = \frac{1}{\mu_f} \frac{\sigma^*{}_r(1 + \sin\phi') - \sigma^*{}_a(1 - \sin\phi')}{k_r(1 + \sin\phi') - k_a(1 - \sin\phi')} \tag{34}$$

Thus, if we know the experimental values of $\sigma^*{}_r$, $\sigma^*{}_a$ at failure, it is possible to calculate the values of σ_f^L using (34). These back-analysed values of σ_f^L can be plotted versus the recorded mean isotropic stress at failure (also available from the experimental results) as shown in Figure 9. The parameters a_{sf} and δ_{sf} can be calibrated so that (18) fits the back-analysed data as shown in Figure 9. The procedure has been applied only to samples reinforced with fibres (2) and (3) because, unlike fibre (1), they showed failure conditions in the stress–strain plots. Although the parameters a_{sf} and δ_{sf} for fibre type (3) appear to be compatible with a slip mode fibre/sand failure mechanism, those for fibre (2) suggest the existence of a much more complex failure mechanism.

Typically, over a wide range of stresses, sand reinforced with randomly distributed discrete fibres exhibits either curved-linear or bilinear failure envelopes ([26] and [27] among others). Above a threshold confining stress, σ_{crit}, the failure envelopes for the reinforced sand become parallel to the unreinforced sand envelope and the failure mechanism is caused by the yielding or breakage of fibres. Below σ_{crit}, it is considered that the tensile resistance of the fibres is not fully mobilized during shearing, but the fibres tend to slip or pull out. The failure envelopes for sand samples

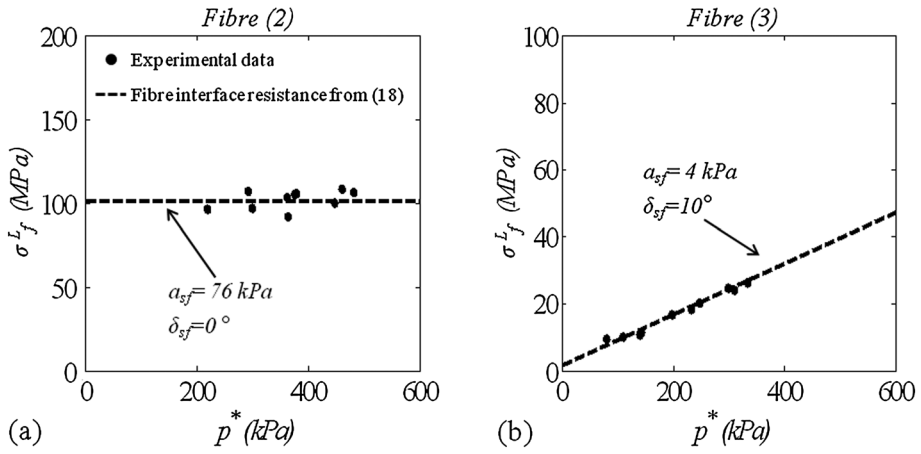

Figure 9. Calibration of the parameters a_{sf} and δ_{sf} of σ_f^L for (a) monofilament fibres and (b) platy fibres.

DOI: 10.1002/nag

reinforced with both fibre types (2) and (3) are shown in Figure 10a and b, respectively. The comparison of the failure envelopes for sand unreinforced and reinforced with fibre type (3) in Figure 10b confirms that for the imposed stress range, the failure occurs in the slip mode. For fibre type (2), although no sign of plastic straining or breakage of the fibres was visible on the exhumed samples, the failure envelopes of the reinforced sand are parallel to the one of the unreinforced soil (Figure 10a). Moreover, the back-analysed limit value of the stress in the fibre (about 100 MPa in Figure 9a) is well below the yielding threshold obtained from single fibre tensile test (Figure 7). Parallel failure envelopes between unreinforced and fibre reinforced sands, with absence of yielding or rupture of the reinforcing glass fibres have also been reported by Maher and Gray (1990) [27]. The occurrence of sand arching around the fibres, as suggested by Michałowski (2008) [15], may explain these trends and could be at the origin of the absence of the frictional component in the calibrated fibre/sand interface parameters for fibres (2) (a_{sf} =76 kPa and δ_{sf} =0°). In these conditions, it has to be noticed that a_{sf} and δ_{sf} may cease to have the physical significance attributed by the relationship (17). The sand arching mechanism may be affected by the relative grain to fibre size, but further research is required to clarify this issue.

8.2. *Initial orientation of fibres*

Diambra *et al*. (2007) [14] and Ibraim *et al*. (2012) [18] have demonstrated that the employed moist tamping technique for sample preparation produces a preferred horizontal bedding of fibres and that the distribution of fibre orientation in the investigated specimens can be successfully represented by

$$\rho_{\theta\alpha} = (A_{\theta\alpha} + B_{\theta\alpha}|\cos^{n_{\theta\alpha}}\theta|) \tag{35}$$

where $A_{\theta\alpha}$, $B_{\theta\alpha}$ and $n_{\theta\alpha}$ are constant coefficients linked by (12) and were chosen to be $A_{\theta\alpha}=0$, $n_{\theta\alpha}=5$ and $B_{\theta\alpha}=0.324$ for fibres (1) and (2), whereas $A_{\theta\alpha}=0$, $n_{\theta\alpha}=12$ and $B_{\theta\alpha}=0.467$ for fibres (3). A representation of the determined fibre orientation is given in respect to the horizontal and vertical plane in Figure 11 for all the three fibre types. It is clear that both the assumed orientations denote a strongly preferred horizontal bedding with 83% of fibres oriented between ±30° for fibres type (1) and (2) and 95% for fibres type (3).

8.3. *Model performances*

8.3.1. Typical simulations. Typical simulations of drained compression and extension triaxial tests are presented in q^* - ε_q and ε_p - ε_q planes for effective cell pressures (p_c^*) of 100 kPa (Figure 12). The simulated tests have been performed on very loose specimens with a nominal relative density $D_r \approx 0\,\%$. The model simulations are represented by the thick continuous lines, whereas the experimental data are represented with thin dashed lines. The model simulations match satisfactorily the experimentally observed behaviour in both the stress–strain and volumetric plan for all the three types of reinforcement. All the main experimental observations in section 3 are well reproduced. Slight inaccuracy can be observed in the reproduction of the rather parabolic stress–strain curve

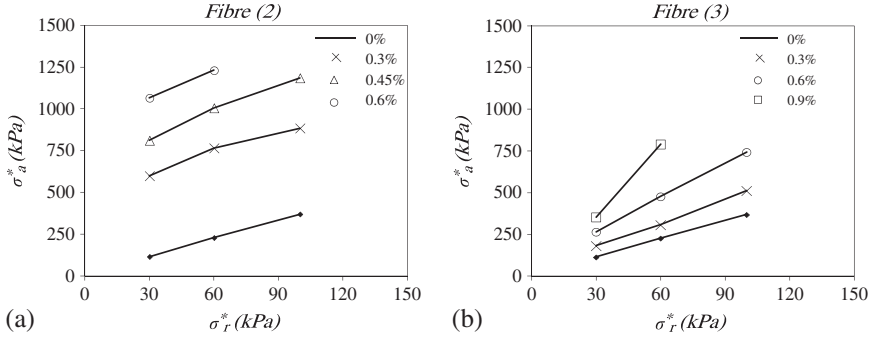

Figure 10. Failure envelopes for samples reinforced with (a) monofilament fibres and (b) platy fibres.

DOI: 10.1002/nag

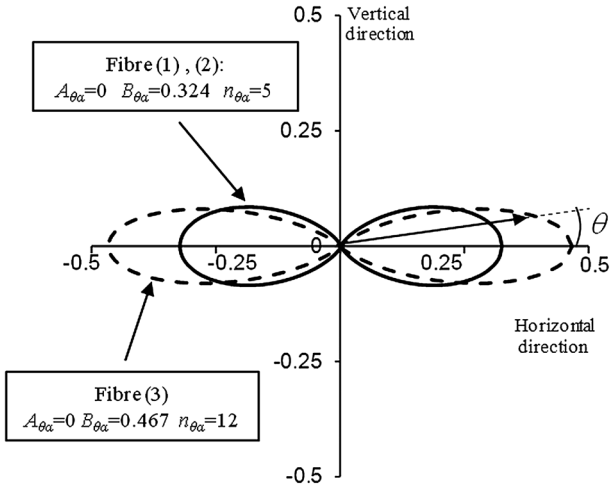

Figure 11. Representation on a vertical plane of the fibre orientation probability function according to (35) with $A_{\theta\alpha}=0$, $n_{\theta\alpha}=5$ and $B_{\theta\alpha}=0.324$ for fibres (1) and (2) and $A_{\theta\alpha}=0$, $n_{\theta\alpha}=12$ and $B_{\theta\alpha}=0.467$ for fibres (3).

shape of the specimens reinforced with fibres (3). Unlike the others, this type of fibres has non-negligible compressive and bending stiffnesses, which are not taken into account in the model.

Simulations of drained compression tests at different confining pressures on loose unreinforced specimens are shown in Figure 13. The stress–strain responses are presented in the q^*/p^*-ε_q plane for unreinforced samples and all types of reinforced samples. For the unreinforced specimens, the experimental q^*/p^*-ε_q trends are rather similar irrespective of the confining pressure. This is reproduced in the model simulations, although the computed response appears slightly stiffer (Figure 13a) when compared with the experimental behaviour. For the reinforced samples (Figure 13b,d), the experimental stress ratio-strain responses do not fall on a unique line, but the stress ratio reduces with increase of confining pressure. The simulations capture this behavioural feature. The contribution of fibres is largely strain dependent and only marginally affected by the confining stress level through the function f_b in (16) and, thus, is more important at low rather than high stress levels. The responses of the reinforced samples do not tend towards a unique q^*/p^* value at large strains because, although the strength of the sand matrix is governed by some sort of frictional relationship, the limiting fibre contribution depends also on the cohesive component a_{sf}. Only if $a_{sf}=0$, then the strength of the reinforced sample would be purely frictional, and a unique asymptotic value of q^*/p^* would be found for each reinforcement type.

Typical comparison between observed and computed behaviour at different specimen densities is shown in Figure 14 for the reinforced specimens with all three types of fibres (w_f = 0.3%). The model captures the strength increase associated with the specimen relative density (Figure 14 a, c, e). The strength increase with the sample relative density comes partly from the density dependent behaviour of the sand matrix and partly from the stress contribution of the fibres. Dense specimens tend to dilate more than loose ones, inducing a greater desire for tensile radial strain and, therefore, greater tensile stresses in the fibres. These create an increased confinement on the sand and, hence, a much larger strength than observed for loose specimens.

At large strains, unreinforced specimens tend towards a limiting critical state strength. For samples reinforced with fibre type (1), such a critical state is not reached because the fibre reinforced sample does not reach failure. For the samples reinforced with fibre type (2) and (3), specimens at different relative density do not reach exactly the same deviatoric strength at large strains. Because the fibre content is expressed in terms of weight ratio, the volumetric concentration of fibres increases slightly with sample density, and the denser samples should reach a slightly stronger critical state. Silva Dos Santos *et al.* (2010) [30] suggested that the mechanical behaviour of fibre-reinforced sands follow a critical state framework, and these simulations do not conflict with this proposition. As expected, denser reinforced samples reach their failure state

DOI: 10.1002/nag

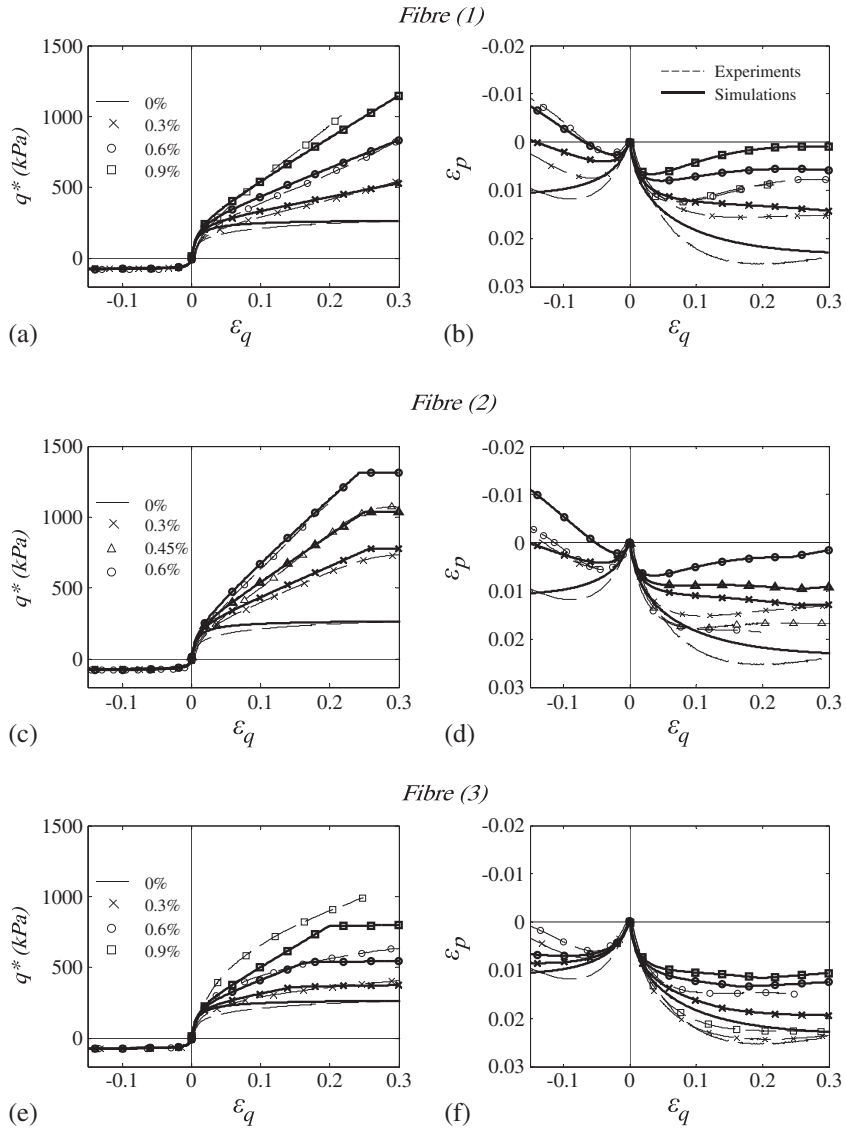

Figure 12. Triaxial test results and model simulations for *(L)* series specimens at 100 kPa cell confining pressure (legend indicates the fibre content).

before looser samples (Figure 14 c and e) as the increased desire to dilate leads to increased fibre pullout.

The simulated volumetric strains are satisfactory but, in detail, are more accurate for denser specimens for which any unrecorded variation of relative density during sample fabrication or installation is less critical for the volumetric behaviour.

9. DISCUSSION

9.1. The effective stress paths followed by the fibres and sand matrix

The evolution of the predicted stress state for the reinforced material, the sand matrix and the fibre phase are illustratively analysed in this section for samples reinforced with fibre (2). External constraints require the reinforced soil to follow the conventional $\delta q^*/\delta p^* = 3$ stress path whether loaded in compression or extension (Figure 15). According to (7), any stress state of the composite

DOI: 10.1002/nag

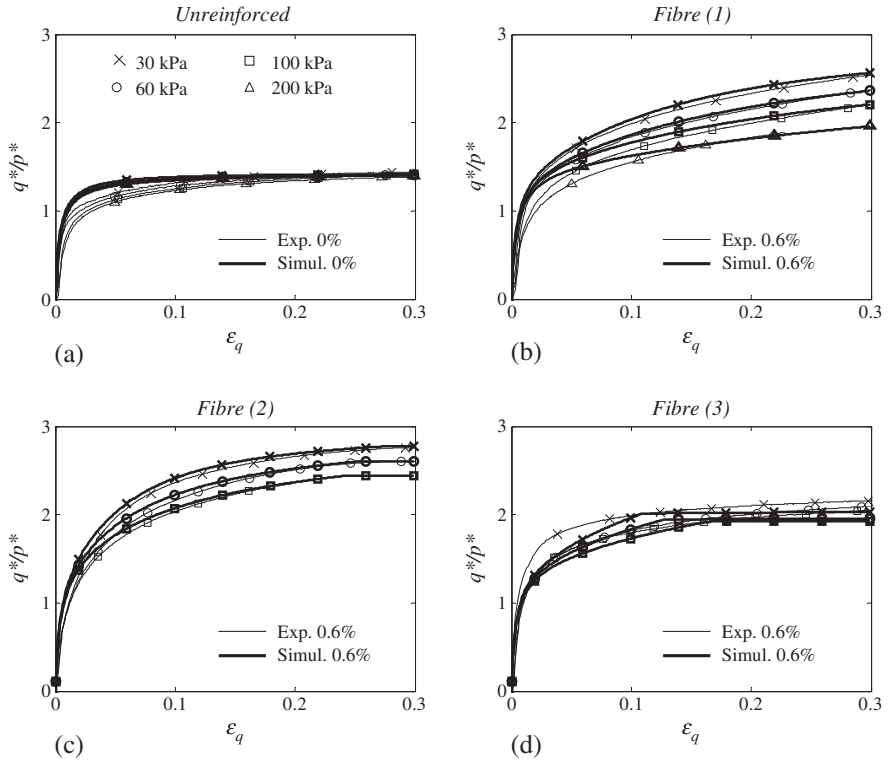

Figure 13. Triaxial test results and model simulations for *(L)* series unreinforced and reinforced (0.6%) specimens (legend indicates the effective preconsolidation pressure).

($\boldsymbol{\sigma}^*$) is computed from the volume weighted summation of the stress states in the fibres $\left(\mu_f \overline{\boldsymbol{\sigma}}_f\right)$ and the sand matrix ($\mu_m \boldsymbol{\sigma}'$). The fibre contribution is shown in Figure 15 as an upward arrow in compression and downward arrow (although not clearly visible for the limited contribution of the fibres) in extension: the fibres always carry a negative (tensile) mean stress, whereas the deviatoric stress is positive in compression and negative in extension.

Because of the stresses contributed by the fibres, the stress path of the sand matrix follows a rather non-conventional stress path. For compressive loading, at the early stage, it is almost coincident with the one of the unreinforced soil but then gradually diverges to climb along the critical state line at large strains — the sand matrix must asymptotically reach the critical state when sheared monotonically. The sand is able to climb up the critical state line because the continuing straining generates a continuing increase in fibre stress contribution. The two components $\mu_f \bar{p}_f$, $\mu_f \bar{q}_f$ of the fibre stress increase almost linearly during the tests as shown in Figure 16a. This linearity of the stress–strain behaviour of the fibres may explain the corresponding linear trend of the stress–strain response for the reinforced soil at medium large strains (Figure 16b). Figure 16b shows the comparison between the stress–strain behaviour of the reinforced soil and that for the sand matrix: the model suggests that the sand matrix is supporting most of the deviatoric strength as a result of the increasing confining stress provided by the fibres. However, at large strains, the fibre stress contribution may reach its allowable limit if pullout takes place. After pullout, both the fibre stress contribution and the stress state of the sand matrix remain constant (see Figure 16a and b, respectively), and the reinforced sample has reached failure (Figure 16b).

9.2. The orientation of fibres and anisotropic response

The model can evidently accommodate any form of fibre orientation, and we will briefly explore the influence of fibre orientation on the simulated response. Three distributions will be considered: preferred horizontal, isotropic and preferred vertical fibre orientation. The distribution of orientation

DOI: 10.1002/nag

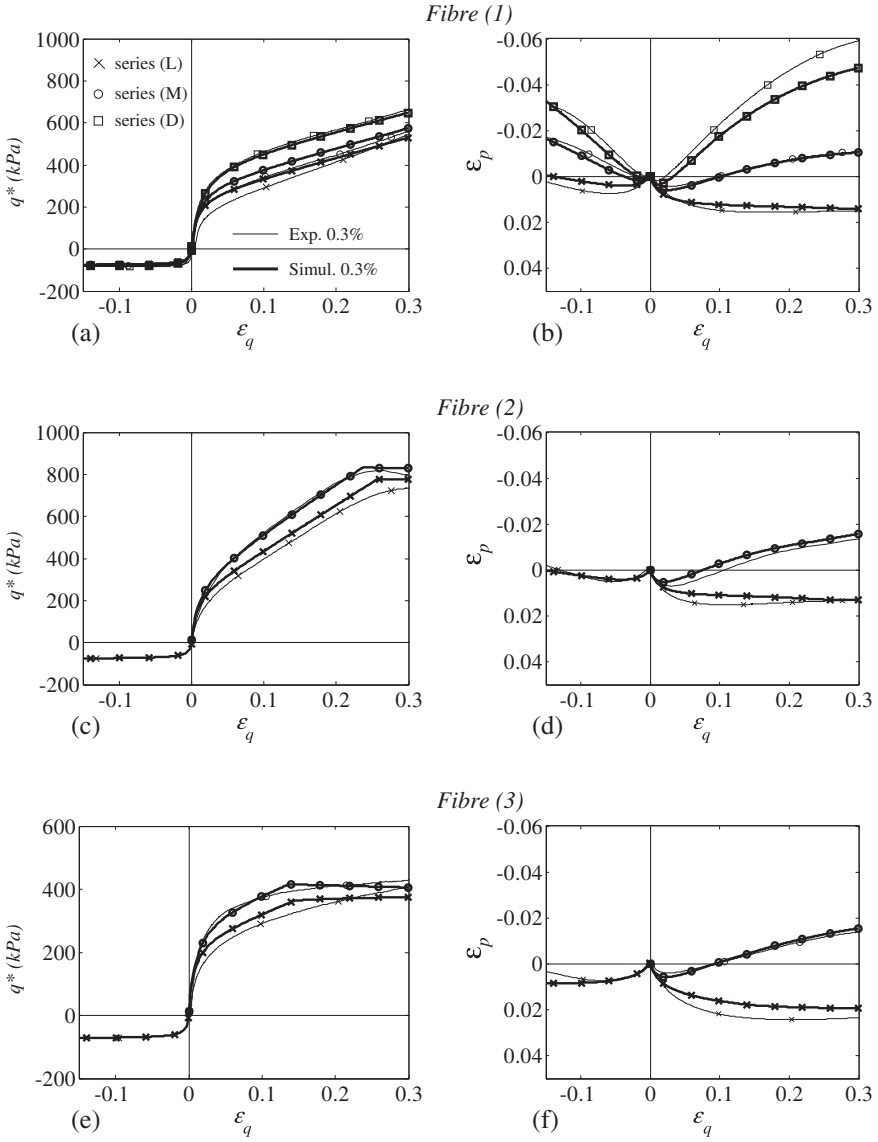

Figure 14. Triaxial test results and model simulations unreinforced and reinforced (0.3%) specimens preconsolidated at 100 kPa (legend indicates specimens nominal densities).

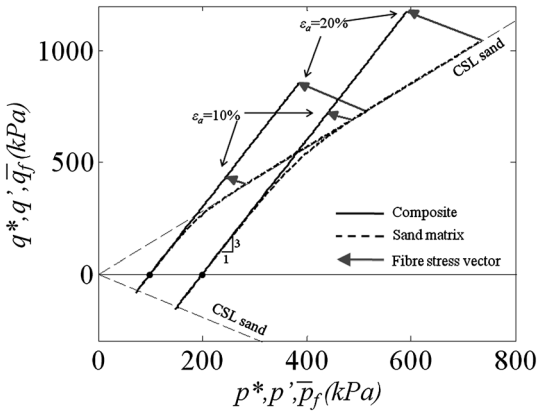

Figure 15. Sand matrix and fibres contribution to the composite stress state for specimen reinforced with fibre (2) at 0.6% fibre content and preconsolidated to 100 and 200 kPa.

DOI: 10.1002/nag

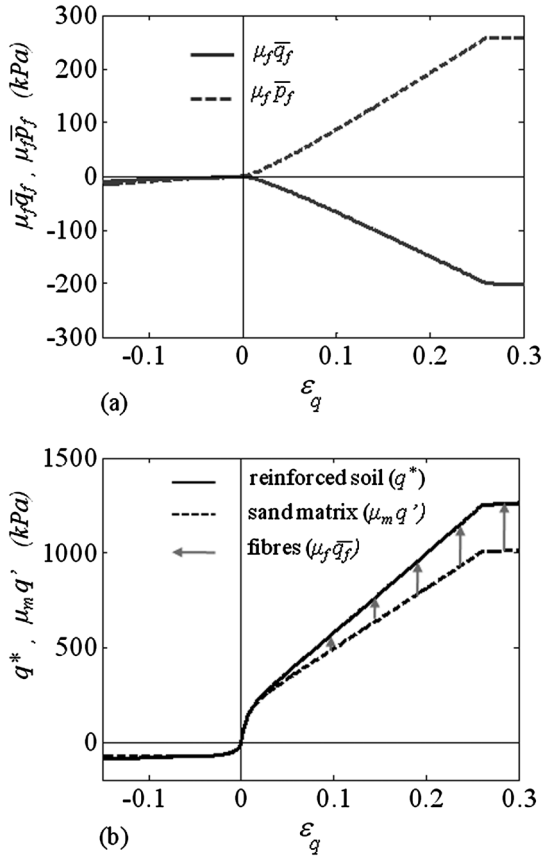

Figure 16. (a) Typical evolution of stress in the fibres (type 2) for compression and triaxial test. (b) Typical deviatoric stress–strain contribution of the fibres and sand matrix.

for fibre type (1) has been selected as preferred horizontal orientation. The preferred vertical orientation has been arbitrarily chosen as a vertical ellipse having a major axis with length similar to the preferred horizontal:

$$\rho_{\theta\alpha} = (A_{\theta\alpha} + B_{\theta\alpha}|\sin^{n_{\theta\alpha}}\theta|) \tag{36}$$

where $A_{\theta\alpha}=0$, $n_{\theta\alpha}=1$ and $B_{\theta\alpha}=0.318$.

Simulations have been performed for triaxial compression and extension tests at constant mean effective pressure ($p^*=50$ kPa), and all the other model parameters defined for fibre type (1) have been assumed. The use of a constant effective stress path eliminates any pressure dependence of the parameter f_b. The results are presented in terms of deviatoric stress–strain behaviour and volumetric behaviour in Figure 17, whereas Figure 18 shows the stress paths for the three assumed orientations.

In the deviatoric stress–strain plot (Figure 17a), the vertical preferred orientation of fibres results in an opposite anisotropy of strength if compared with the horizontal orientation. The isotropic fibre orientation produces an almost identical strength for compression and extension: the reinforcing contribution of fibres is strain dependent, and the different deformation patterns associated with triaxial compression and extension (as shown in the volumetric plots in Figure 17b) do not produce perfect isotropy of strength. The slight difference of fibre contribution for compression and extension is more clearly seen in Figure 18b, where the fibre stress vector seems slightly longer and more inclined for extension. At 20% deviatoric strain, the stress contribution of the isotropic distribution of fibre orientations has a slope of -50.1° in the $\bar{q}_f - \bar{p}_f$ plane for compressive loading and 62.4° for extension (Figure18b). The slope of the stress contribution of the fibres changes also slightly during the test: it is influenced by the evolution of the tensile strain domain.

DOI: 10.1002/nag

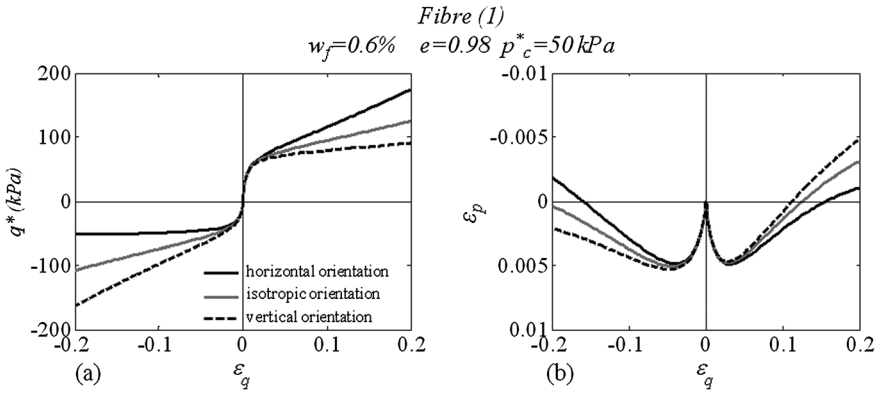

Figure 17. Comparison of model simulations adopting a preferred horizontal, isotropic and preferred vertical fibre orientation for triaxial compression and extension tests at constant mean effective pressure of 50 kPa: (a) deviatoric stress–strain (b) volumetric plot.

The volumetric behaviour is not so dramatically affected by the fibre orientation. The densification resulting from the occupation of voids in the soil with fibrespace leads to increased dilation, but the fibres contribute higher stresses, implying a competing more compressive behaviour of the fibre reinforced sample (Figure 17b). For compression loading, the more compressive behaviour is shown for horizontal fibre orientation, whereas for extension loading, the vertical fibre orientation shows greater compression.

Overall, these simulations demonstrate the central role played by the anisotropic nature of fibre orientation on the strength of the reinforced sample. For perspective field applications of fibre-reinforced sands, especially when rotation of principal axes of stress or strain can occur, it appears extremely important to estimate the actual distribution of fibre orientations.

9.3. Reinforcing effectiveness: fibre stiffness and fibre/sand surface interaction

According to (23), for a fixed level of strain the stress mobilized in the fibres is proportional to both the elastic modulus E_f and the efficiency factor K_e, and thus, the fibres reinforcing effectiveness is governed by the product $E_f * K_e$. Figure 19 shows the relative magnitude of these parameters for the three fibres. It is clear that, although fibre (2) has not the highest E_f nor K_e, it is the most effective reinforcement (compare the mobilized strength values reported in Table III for all the fibres) because of the biggest $E_f * K_e$ value. The effectiveness of fibres seems governed by the elastic modulus, fibre/sand interaction compromise.

Although the elastic modulus of the fibres can be determine through a simple tension test on the fibre, the parameter K_e cannot be easily determined with an experimental procedure. Actually, K_e can be a convenient macro-scale parameter, which accounts for the interaction of fibres and sand grains at the micro-scale level and may also take into account for non-uniform strain distribution along the fibre especially at its extremities. K_e is expected to be directly linked to the soil (e.g. grain size and gradation) and the fibre (e.g. shape, aspect ratio, material, surface roughness) characteristics [[2, 4, 27] among others]. The calibration of the constitutive model parameters can provide useful information on the fibre/sand interaction, which may substitute direct and sophisticate experimental investigation.

Among other factors, it appears that the tendency of the fibres to tangle around the soil highly influences K_e. Fibres (1) are crimped and have also negligible bending stiffness, which facilitates to get entwined with the soil and, in turn, improve the grip between fibres and soil grains. Although fibres (2) are not crimped, they still have a negligible bending stiffness, which enables them to get entwined in the soil but probably at a less proportion as shown by the respective values of K_e in Figure 19. Nevertheless, fibres (1) and (2) have a rather similar value of K_e, whereas fibres (3), which possess higher bending stiffness that prevents them to bend around the soil grains, have a much lower value.

DOI: 10.1002/nag

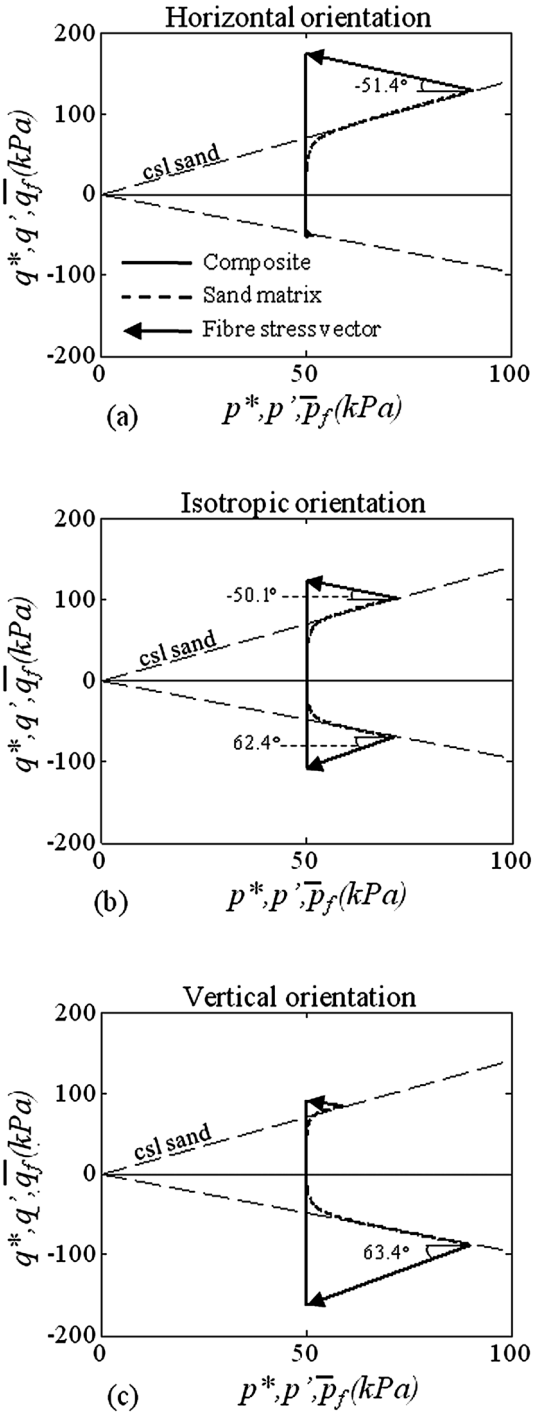

Figure 18. Comparison of computed stress path for the reinforced soils adopting (a) preferred horizontal, (b) isotropic and (c) preferred vertical fibre orientation for triaxial compression and extension tests at constant mean effective pressure of 50 kPa.

9.4. Fibrespace: the volume of voids 'attached' to the fibres

Model simulations for a loose sample ($D_r \approx 0\,\%$) reinforced with 0.6% of fibre type (1) and considering only the solid volume occupied by the fibres (assuming that the fibre specific volume $v_f = 1$ with no voids 'stolen' from the sand matrix) are shown in Figure 20. Although the stress–strain behaviour is

DOI: 10.1002/nag

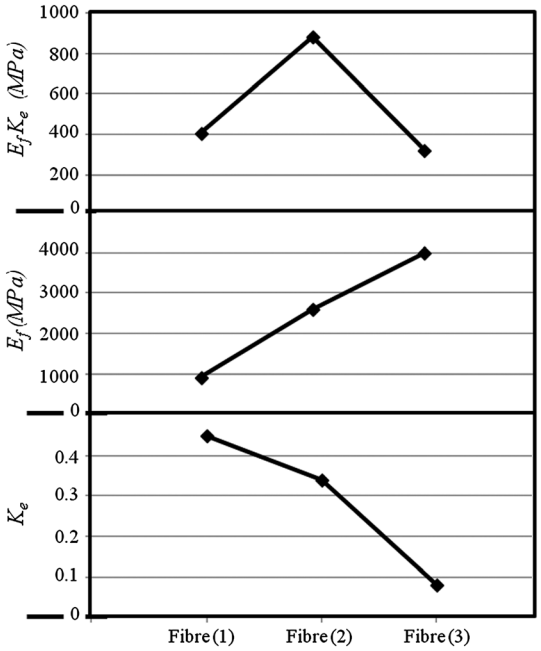

Figure 19. Comparison of parameters governing the reinforcing effectiveness of the fibres, K_e, E_f and the product K_e E_f for the three types of fibre.

quite well simulated (Figure 20a), the predicted volumetric behaviour is much more compressive than experimentally observed (Figure 20b) for both compression and extension. For the compressive case, the computed volumetric behaviour shows a continuous linear compression, which contrasts with the small dilation observed experimentally. The continuous compression is related to the progressive increase of the confinement stress provided by the fibres as they are stretched (Figure 16a). In extension, the continuous compression is not observed because of the negligible stress contribution of the fibres for this particular loading orientation. Nevertheless, the predicted behaviour is not as dilative as experimentally observed. The analysis of these volumetric simulations suggests that the fibre-sand matrix interaction is not limited to stresses exchanged at the interface between fibre and soil: another mechanism is required.

Previous studies on fibre reinforced concrete have demonstrated that the presence of fibres can perturb the packing of the neighbourhood granular structure as the grain particles are restrained from assuming their preferred configuration because of the fibre presence: the packing density of the grains may decrease significantly near the fibres [31]. De Larrard (1999) [32] suggested that

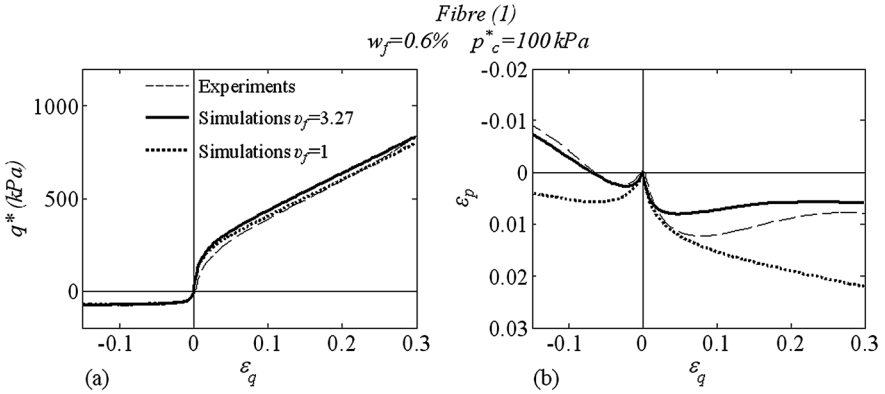

Figure 20. Influence of the fibre specific volume on the model simulations for a sample reinforced with 0.6% fibre (1) under triaxial compression and extension loading at 100 kPa cell confining pressure.

DOI: 10.1002/nag

the local decrease in relative density in the vicinity of the fibre is induced by the fact that some of the voids around the fibre shaft cannot be occupied by the grains. Thus, a similar approach to the one suggested by De Larrard (1999) [32] is introduced here by assigning some of the available voids to the fibre phase (or allowing that the specific volume of the fibres v_f can be greater than unity) and preventing the sand matrix to use these voids during loading. In this way, the sand matrix feels itself to be in an averaged denser state (the overall specific volume v_m is less than in the previous case) and, hence, to have an increased desire for dilation, which opposes the compressive tendency induced by the confining stress generated by the fibres. Model simulations imposing a specific volume of the fibres $v_f = 3.27$ are proposed also in Figure 20b. The computed volumetric behaviour now matches the experimental response quite satisfactorily. In this case, the specific volume of the sand matrix has changed from $v_m = 1.93$ (for $v_f = 1$) to $v_m = 1.89$ (for $v_f = 3.27$) with an increase of relative density D_r from 18.9% to 29.7%. Such a modelling ingredient is effective only if coupled with a sand model which can adequately represent the fundamental density dependence of the mechanical behaviour of granular soils.

10. CONCLUSION

Based on experimental evidence, a new constitutive model for fibre reinforced sands has been developed. At the scale of typical geotechnical systems, it is desirable to model the fibre/soil mixture as a single material or continuum because the vehicle for their use in design and predictive analyses is invariably a continuum numerical program. The constitutive model is built on the superposition of the stress and strain states of the sand matrix and fibres. The model considers that the sand matrix obeys its own constitutive laws: the Severn-Trent sand model has been adopted. The fibres are considered as discrete forces with defined orientation. The divergence theorem has been employed to determine their equivalent continuum stress contribution, which could be then superimposed onto that of the sand matrix. The modelling of the fibres requires the calibration of only three additional model ingredients: a fibre-sand bonding efficiency factor, the pull-out resistance of the fibres and their specific volume, whereas the adopted model for the sand matrix necessitates ten model parameters. The model is successful in capturing some of the key aspects related to the fibre/sand interaction mechanisms like fibre content and orientation, relative fibre/sand slippage and pullout mechanisms, apparent densification matrix effect induced by the presence of fibres and strain level dependency. The model has been challenged and produced satisfactorily simulations for sand reinforced with three different types of fibres in axi-symmetric loading conditions and different stress and density levels. Although the model can effectively be employed as a tool to further explore the complexities of the internal fibre/sand interaction mechanisms, it is also an accessible tool for predictive and design analyses of geotechnical systems. Current ongoing developments involve extension of the model formulation in the generalized multiaxial space and implementation and validation in a commercial finite element numerical code.

REFERENCES

1. Koerner RM, Welsh JP. *Construction and geotechnical engineering using synthetic fabrics*. New York, NY: Wiley Series of Practical Construction Guides, 1980.
2. Gray DH, Al-Refeai TO. Behaviour of fabric - versus fiber-reinforced sand. *Journal of Geotechnical Engineering ASCE* 1986; **112**(8):804–820.
3. Michałowski RL, Zhao A. Failure of fiber-reinforced granular soils. *Journal of Geotechnical Engineering ASCE* 1996; **122**(3):226–234.
4. Michałowski RL, Čermák J. Triaxial compression of sand reinforced with fibers, *Journal of Geotechnical and Geoenvironmental Engineering* ASCE. 2003; **129**(2):125–136.
5. Consoli NC, Casagrande MDT, Coop MR. Performance of a fibre-reinforcedsand at large shear strains. *Geotechnique* 2007; **57**(9):751–756.
6. Diambra A, Ibraim E, Muir Wood D, Russell AR. Fibre Reinforced Sands: Experiments and Modelling. *Geotextiles and Geomembranes* 2010; **28**:238–250. doi:10.1016/j.geotexmem.2009.09.010.
7. Ibraim E, Diambra A, Muir Wood D, Russell AR. Static liquefaction of fibre reinforced sand under monotonic loading. *Geotextiles and Geomembranes* 2010; **28**:374–385. doi:10.1016/j.geotexmem.2009.12.001.

DOI: 10.1002/nag

8. Lirer S, Flora A, Consoli NC. On the strength of fibre-reinfroced soils. *Soils and Foundations* 2011; **51**(4):601–610.
9. Ibraim E, Muir Wood D, Maeda K, Hirabayashi H. Fibre-reinforced granular soils behaviour: numerical approach. *Proceedings of the International Symposium on Geomechanics and Geotechnics of Particulate Media*, Ube, Yamaguchi, Japan 2006; **12–14**:443–448.
10. Maeda K, Ibraim E. DEM analysis of 2D fibre-reinforced granular soils. *Proceedings of the International Symposium on Deformation Characteristic of Geomaterials*, IS-Atlanta 2008; **2**:623–628.
11. Villard P, Jouve P, Riou Y. Modélisation du compertment mécanique du Texsol. *Bulletin Liaison Laboratoire Central des Ponts et Chaussées* 1990; **168**:15–27.
12. di Prisco C, Nova R. A constitutive model for soil reinforced by continuous threads. *Geotexiles and Geomembranes* 1993; **12**(2):161–178.
13. Gajo A, Muir Wood D. Severn-Trent sand: a Kinematic-hardening constitutive model: the q-p formulation. *Geotechnique* 1999; **49**(5):595–614.
14. Diambra A, Russell AR, Ibraim E, Muir Wood D. Determination of fibre orientation distribution in reinforced sand. *Geotechnique* 2007; **57**(7):623–628. doi:10.1680/geot.2007.57.7.623.
15. Michałowski RL. Limit analysis with anisotropic fibre-reinforced soil. *Geotechnique* 2008; **58**(6):489–501.
16. Diambra A, Ibraim E, Russell AR, Muir Wood D. Modelling the undrained response of fibre reinforced sands. *Soils and Foundations* 2011; **51**(4):625–636.
17. Ang EC, Loehr JE. Specimen size effects for fiber-reinforced silty clay in unconfined compression. *Geotechnical Testing Journal* 2003; **26**(2):1–10.
18. Ibraim E, Diambra A, Russell AR, Muir Wood D. Assessment of laboratory sample preparation for fibre reinforced sands. *Geotextiles and Geomembranes* 2012; **34**:69–79.
19. Ibraim E, Fourmont S. Behaviour of sand reinforced with fibres. In *Soil Stress–strain Behaviour: Measurement, Modelling and Analysis*, Ling *et al*. (eds.). Springer, 2006; 807–818.
20. Michałowski RL, Čermák J. Strength anisotropy of fiber-reinforced sand. *Computers and Geotechnics* 2002; **29**:279–299.
21. Heineck CS, Consoli NC, Coop MR. Effect of microreinforcement of soils from very small to large shear strains. *Journal of Geotechnical and Geoenvironmental. Engineering* ASCE. 2005; **131**(8):1024–1033.
22. Roscoe KH, Schofield AN. Mechanical Behaviour of an idealised "Wet-Clay", *Proceedings of the European Conference on Soil Mechanics and Foundation Engineering*, Wiesbaden. 1963; **1**:47–54.
23. Been K, Jefferies MG. A state parameter for sands. *Geotechnique* 1985; **35**(2):99–112.
24. Diambra A. Fibre Reinforced Sands: Experiments and Modelling. *PhD Thesis*, University of Bristol, UK, 2010.
25. Machado SL, Carvalho MF, Vilar O. Constitutive model for municipal solid waste, *Journal of Geotechnical & Geoenvironmental Engineering*, ASCE. 2002; **128**(11):940–951.
26. Gray DH, Ohashi H. Mechanics of fiber reinforcement in sands, *Journal of Geotechnical Engineering*, ASCE. 1983; **109**(3):335–353.
27. Maher MH, Gray DH. Static response of sand reinforced with fibres, *Journal of Geotechnical Engineering*, ASCE. 1990; **116**(11):1661–1677.
28. Zornberg JG. Discrete framework for equilibrium analysis of fibre-reinforced soil. *Geotechnique* 2002; **52**(8):593–604.
29. Hardin BO, Black WL. Sand stiffness under various triaxial stress, *Journal soil Mechanics and Foundation Division* ASCE. 1966; **SM**:353–369.
30. Dos Santos APS, Consoli NC, Baudet BA. The mechanics of fibre-reinforced sand. *Geotechnique* 2010; **60**(10):791–799.
31. Bartos PJM, Hoy CW. Interaction of particles in fibre reinforced concrete. In *Production Methods and Workability of Concrete*. E&FN Spon: London, 1996; 451–461.
32. de Larrard F. Concrete Mixture Proportioning: A Scientific Approach. In *Modern Concrete Technology Series*. SPON: London, 1999.

DOI: 10.1002/nag